RESEARCH ARTICLE

VOLCANICA

# Textural complexity and geochemistry on the last millennium pyroclastic deposits from Puyehue-Cordón Caulle Volcanic Complex, Chile: Implications for tephrochronological and volcanological interpretations

Walter Alfonzo*[α,β], Romina Daga[α,β], Alejandro Demichelis[γ], Gastón Goldmann[α], and Sergio Ribeiro Guevara[α]

[α] Laboratorio de Análisis por Activación Neutrónica, Centro Atómico Bariloche, Comisión Nacional de Energía Atómica, Av. Bustillo Km 9.5, 8400 San Carlos de Bariloche, Argentina.

[β] Centro Científico Tecnológico CONICET Patagonia Norte, Avenida de Los Pioneros 2350, 8400 San Carlos de Bariloche, Argentina.

[γ] Departamento de Geología, Universidad Nacional de Río Cuarto. Instituto de Ciencias de la Tierra, Biodiversidad y Sustentabilidad Ambiental, CONICET-UNRC, Ruta Nacional N°36 km 601, Río Cuarto, Argentina.

Submitted: 2023-11-08 | Accepted: 2024-12-13 | Published: 2025-02-21

Editor: J. Farquharson | Typesetter: E. Hughes

## Abstract

The component variability in Puyehue-Cordón Caulle Volcanic Complex (PCCVC) products reflects the inherent complexity of volcanic processes. We examine pyroclastic deposits from Cordón Caulle (2011 and 1960 eruptions) and Puyehue (MH tephra) in a profile ~20 km windward of the PCCVC. All levels have comparable components (pumice, scoria, glass shards, crystals), but their proportions vary according to the dominant eruptive style in both vent sources. The particle microtextures combined with mineralogy and geochemistry differentiate juvenile from non-juvenile particles in macroscopically undifferentiated components, questioning prior assumptions. Highly vesicular pumice is the dominant juvenile component indicating decompression-driven gas exsolution processes. Juvenile blocky glass shards/obsidians, frequently associated with lithics, now provide insights into the potential higher involvement of magma in the phreatomagmatic phases of the MH deposit. Nevertheless, the variability of tephra components is a characteristic of the PCCVC, regardless of the juvenile or lithic character. This research refines tephrochronological tools and deepens our understanding of volcanic processes and deposits in the PCCVC.

## Resumen

La variabilidad de componentes en los productos del Complejo Volcánico Puyehue-Cordón Caulle (CVPCC) refleja la complejidad inherente de los procesos volcánicos. En este trabajo, examinamos depósitos piroclásticos de Cordón Caulle (erupciones de 2011 y 1960) y Puyehue (tefra MH) en un perfil a ~20 km al sudeste del CVPCC. Todos los niveles presentan componentes comparables (pómez, escoria, fragmentos de vidrio, cristales), pero sus proporciones varían según el estilo eruptivo dominante en ambos centros de emisión. Las microtexturas de las partículas, combinadas con mineralogía y geoquímica, permiten diferenciar partículas juveniles de no juveniles en componentes que son macroscópicamente similares, cuestionando suposiciones previas. La pómez altamente vesiculada es el componente juvenil dominante, lo que indica procesos de desgasificación impulsados por la descompresión. Los fragmentos angulosos de vidrio juvenil/obsidiana, frecuentemente asociados con líticos, ahora aportan información sobre la posible mayor participación de magma en las fases freatomagmáticas del depósito MH. No obstante, la variabilidad de los componentes de la tefra es una característica del CVPCC, más allá del carácter juvenil o lítico. Esta investigación mejora las herramientas de tefrocronología y profundiza nuestra comprensión de los procesos volcánicos y los depósitos en el CVPCC.

Keywords: Tephra; Morphology; Microtexture; Mineralogy; Geochemistry; Southern Volcanic Zone.

## 1 Introduction

The characterization of pyroclastic materials and their association with a specific source (a particular eruption or volcano) is essential to enable the use of tephras as stratigraphic markers on a regional scale. Tephra layers are considered instantaneous deposits in geological times, since large volumes of material generated by explosive volcanic eruptions can be dispersed several hundred kilometres covering different environments in hours or days. This characteristic of tephra deposits, together with the advances in the study of its components, has allowed the development of tephrochronology to support the dating of widespread sedimentary settings [Lowe 2011; Di Roberto et al. 2021; Alloway et al. 2022]. Moreover, the potential for analysing the processes involved in eruption dynamics [Weller et al. 2019; Thivet et al. 2022] further underscores the significance of these advancements in tephra studies.

When possible, the analysis of tephras requires several approaches of study, from the identification of the deposit in the field and its sedimentary features, the internal component and grain size variations, to the microscopic textural and geochemical analysis of the volcanic glass and mineral phases immersed [Lowe 2011]. Determining the concentrations of trace elements is one of the most powerful tools to identify different volcanic sources, relevant for the reconstruction of the eruptive chronology in different sedimentary environments [Lowe et al. 2017; Del Carlo et al. 2018]. In addition, textural characterization also provides information about magmatic processes

* walter.alfonzo@cab.cnea.gov.ar

that occur both in the chamber and during magma ascent to the surface, such as volatile exsolution, magma fragmentation, further recrystallization events, etc. [Platz et al. 2007; Kratzmann et al. 2009; Jones and Russell 2017; Paredes-Mariño et al. 2017; Matsumoto and Geshi 2021]. Also, different volcanic pulses or events of different explosive energies can generate a wide variety of typologies, grain size distributions, textures, and composition of juvenile fragments [Lautze and Houghton 2007; Cioni et al. 2015]. The study of these characteristics in the tephra deposits and the stratigraphic variations can give clues to understanding the eruptive dynamics, allowing one to infer the eruptive style of a volcano and its temporal variations, improving also the information for correlating purposes [Toramaru et al. 2008; Mujin and Nakamura 2014].

The Southern Volcanic Zone (SVZ, 33–46°S) of the Andes comprises numerous volcanoes with activity of variable intensity during the Holocene [Stern 2004]. At these latitudes, particularly, the predominant wind direction from the west occurs 85 % of the year [Paruelo et al. 1998] and allows the dispersion of tephra towards the east. In general, the pyroclastic deposits can be eroded or obliterated by the complexity of the volcanic processes in the proximal area, and complete sequences are rarely preserved within the first kilometers (5–10 km) from the vent. However, in medial positions to the eruptive centers [10–50 km; Cioni et al. 2015], remarkably well-preserved tephra deposits downwind in the forested basins of southern Chile and Argentina have been defined [Naranjo and Stern 1998; 2004; Lara and Moreno 2006; Singer et al. 2008; Stern 2008; Watt et al. 2011; Fontijn et al. 2014; Rawson et al. 2015]. Although several recent studies have shown that the frequency of volcanic activity in this segment is underestimated [Amigo et al. 2013; Rawson et al. 2015; Fontijn et al. 2016], most of the volcanic centers that comprise it have generated large explosive postglacial eruptions. These eruptions produced regional marker deposits, very useful to synchronize medial to distal sedimentary archives.

Among southern Andean volcanoes, the Puyehue-Cordón Caulle Volcanic Complex (PCCVC) is one of the most important due to the frequent activity during the last century and the well-preserved regional tephra fall deposits generated, derived from silicic explosive eruptions [Gerlach et al. 1988; Lara and Moreno 2006]. Recently, tephrostratigraphic studies have reconstructed PCCVC Holocene deposits and characterized them on a regional scale facilitating their identification for long distances [Naranjo et al. 2017; Alloway et al. 2022]. However, with the exception of the studies in products from the Cordón Caulle 2011 eruption, detailed petro-textural studies of the different components of PCCVC tephra layers are still scarce. These deposits represent important chronostratigraphic markers particularly for the last millennium. They provide the opportunity to analyze the volcanic processes involved in the most recent eruptions of this volcanic complex, which combines a fissure system (Cordón Caulle) and a central volcano [Puyehue, Lara and Moreno 2006].

In this study, we characterize the most recent (last millennium) pyroclastic deposits from PCCVC, recovered in medial positions to the volcano. We aim to provide morphological, textural, mineralogical, and geochemical information of the rhyodacitic/rhyolitic material originating from both the Puyehue volcano and the Cordón Caulle fissure system. The primary objective of the detailed characterization is to demonstrate the complexity of the components and to provide data for the correlation of proximal/medial/distal deposits recovered from diverse sedimentary records. Additionally, we seek to elucidate processes involved in the petrogenetic evolution of the studied pyroclasts.

### 1.1 Geological setting and PCCVC regional tephrostratigraphy

Puyehue-Cordón Caulle Volcanic Complex (PCCVC, 40.5°S) belongs to the Northern Patagonia Andean Range, and is one of more than 50 active frontal arc volcanoes that define the 1400 km-long SVZ, the result of the subduction of the Nazca plate below the South American plate (Figure 1). The PCCVC comprises a cluster of ~140 $km^3$ of Pleistocene to Holocene lavas and tephra deposits that outcrop over ~800 $km^2$ [Moreno Roa 1977; Gerlach et al. 1988; Lara et al. 2004; Singer et al. 2008]. The 150 $km^2$ Puyehue composite volcano (2236 m asl, above sea level) comprises ~70 $km^3$ of lavas and tephra [Lara and Moreno 2006; Naranjo et al. 2017]; episodic feeding from a magma reservoir during the last 69 ky has produced ~17 $km^3$ of basaltic to rhyolitic magmas [Singer et al. 2008]. Northwest of the Puyehue composite cone, Cordón Caulle consists of 2 parallel 16 to 20 km long fissures separated by 4 km that form a 120 m deep graben [Moreno Roa 1977; Lara et al. 2004; Lara and Moreno 2006]. The most silica-rich magmas erupted as domes and cones throughout the Cordón Caulle fissure system whereas intermediate compositions dominate on the Puyehue stratocone. Mafic lavas mainly erupted in the early stages along the entire complex [Lara and Moreno 2006], while the last cone eruption, dominantly dacitic, formed the modern 2.5 km diameter crater [Naranjo et al. 2017]. Lately, explosive events were restricted to the Cordón Caulle fissure, with several historical/prehistorical rhyodacite/rhyolite explosive-effusive eruptions.

In the study area, Holocene tephra deposits from PCCVC comprise at least 3 voluminous (~1–8 $km^3$) pyroclastic fall layers, recognizable up to 100 km east of PCCVC [Naranjo et al. 2017]. Main deposits in regional outcrops comprise – following the Naranjo et al. [2017] nomenclature – the oldest Puyehue 1 tephra (10.44–10.49 ky) found at medium-distal facies overlying granitic moraine boulders, consisting of deeply weathered, orange dacitic pumice lapilli; Puyehue 2 deposit (6.71–7.17 ky) comprises dacitic pumice and its age is equivalent to a rhyodacitic dome exposed at the Puyehue summit crater; and the distinctive Mil Hojas (MH) unit, a voluminous multilayered rhyodacitic pumice fall (0.73–1.11 ky), with alternating dark lithic and pumice lapilli beds [Singer et al. 2008; Fontijn et al. 2016; Naranjo et al. 2017; Alloway et al. 2022]. Intercalated with PCCVC tephras there are deposits related to the Antillanca volcanic complex, like the Playa Blanca Negra unit (2.88 ± 0.13 ky), a compositionally-zoned tephra, the Pampa Frutilla Density Current (1.93 ± 0.07 ky), and the Nahuel Huapi Tephra (1.42 ± 0.11 ky), corresponding to a basaltic lithic-rich and scoriaceous fallout deposit [Naranjo et al. 2017]. The PCCVC stratigraphy culminates with several historic Cordón

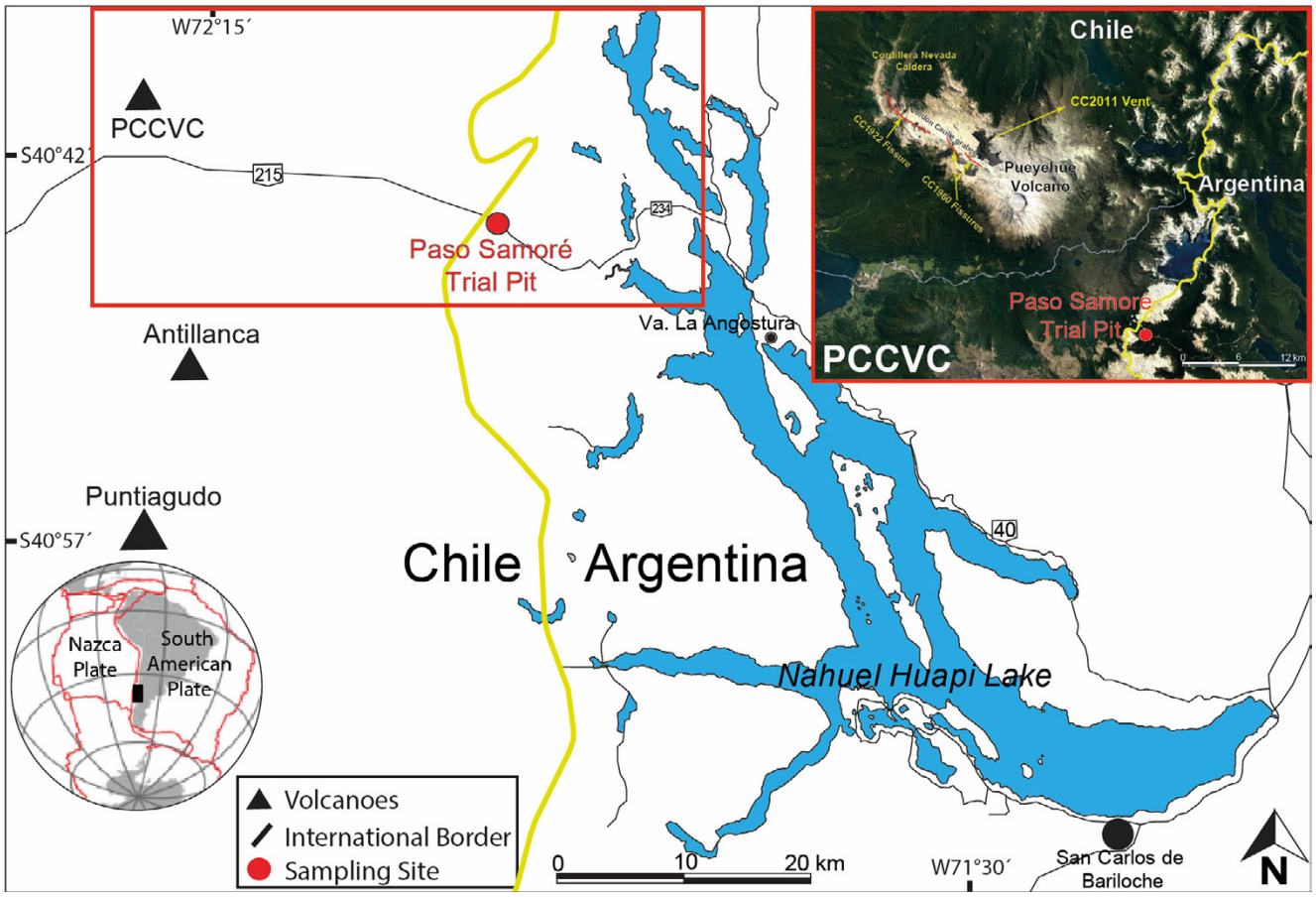


Figure 1: Location map of the sampling site Cardenal Samoré Trial Pit (red dot) and nearest eruptive centers (black triangles): Puyehue-Cordón Caulle Volcanic Complex (PCCVC) and the Antillanca and Puntiagudo-Cordón Cenizos volcanoes. Upper right: a satellite image of the PCCVC with the Pueyehue volcano and the Cordón Caulle fissure system.

Caulle pumice falls during the last centuries. Recently, a deposit from mid-18$^{th}$ century related to the Cordón Caulle system was identified in lake sequences, previously only mentioned in historical chronicles [Lara and Moreno 2006; Sosa et al. 2024]. The last known eruptions correspond to 1921–22, 1960, and 2011. Whilst the 1921–22 and 1960 events represent negligible discrete and discontinuous tephra layers at medial-distal locations, the 2011 eruption completely covered proximal to distal regions to the southeast [Naranjo et al. 2017].

### 1.2 Explosive deposits of the last millennium at PCCVC

The analyses in this study were focused on the events from the last millennium, composed of the last eruption from the Puyehue stratocone and the historical deposits from the Cordón Caulle system, both with extensive dispersion and potential for tephrochronological and volcanological studies. The rhyodacitic Mil Hojas [MH, after Naranjo et al. 2017] deposit is a well-known key marker horizon considering its wide dispersion (up to 120 km east-south east from PCCVC in terrestrial outcrops) and tephra characteristics, with a total volume estimated at 4.3 km$^3$ [Singer et al. 2008; Naranjo et al. 2017; Alloway et al. 2022]. The MH represents the last explosive event from Puyehue volcano, recording several catastrophic subplinian to phreatomagmatic explosions responsible for creating the current summit crater [Singer et al. 2008]. The base of MH was dated at 0.84 ± 0.18 cal ky BP [Fontijn et al. 2016] and between 0.738 ± 0.067 and 1.113 ± 0.068 cal ky BP [Naranjo et al. 2017], extending the possible age of this deposit. The end of MH is marked by an overlying soil, dated at 0.587± 0.081 ky BP [Lara and Moreno 2006]. Recently, the dating of a lake sequence containing the MH tephra constrained the age at 0.736–0.740 cal ky BP [Alloway et al. 2022]. At the selected location (40°43'8"S, 71°56'15"W), in the Paso Cardenal Samoré trial pit (Figure 1), situated approximately 20 km east-southeast from the volcano, the MH deposit is approximately 65 cm thick. This location is intermediate between the profiles from Naranjo et al. [2017], where MH thickness ranges between 45 and 240 cm and almost all subunits defined by such authors were identified (Figure 2). The main characteristic of this multi-layered unit is the marked alternation of generally lapillitic whitish and yellowish pumiceous layers up to 10 cm thick (MH3, MH5, MH7, MH8) with fine to coarse ash dark layers enriched in blocky obsidian and brown glassy fragments (MH1-2, MH4, MH6), as defined by Naranjo et al. [2017]. Other components like brown pumice, black scoria, crystaloclast, and lithics are present in almost all subunits in variable proportions (Figure 3; see Section 3).

Above MH tephra, and separated by an organic-rich level, a centimeter-thick massive level corresponds to the 1960 Cordón Caulle tephra (1960CC). Even though the

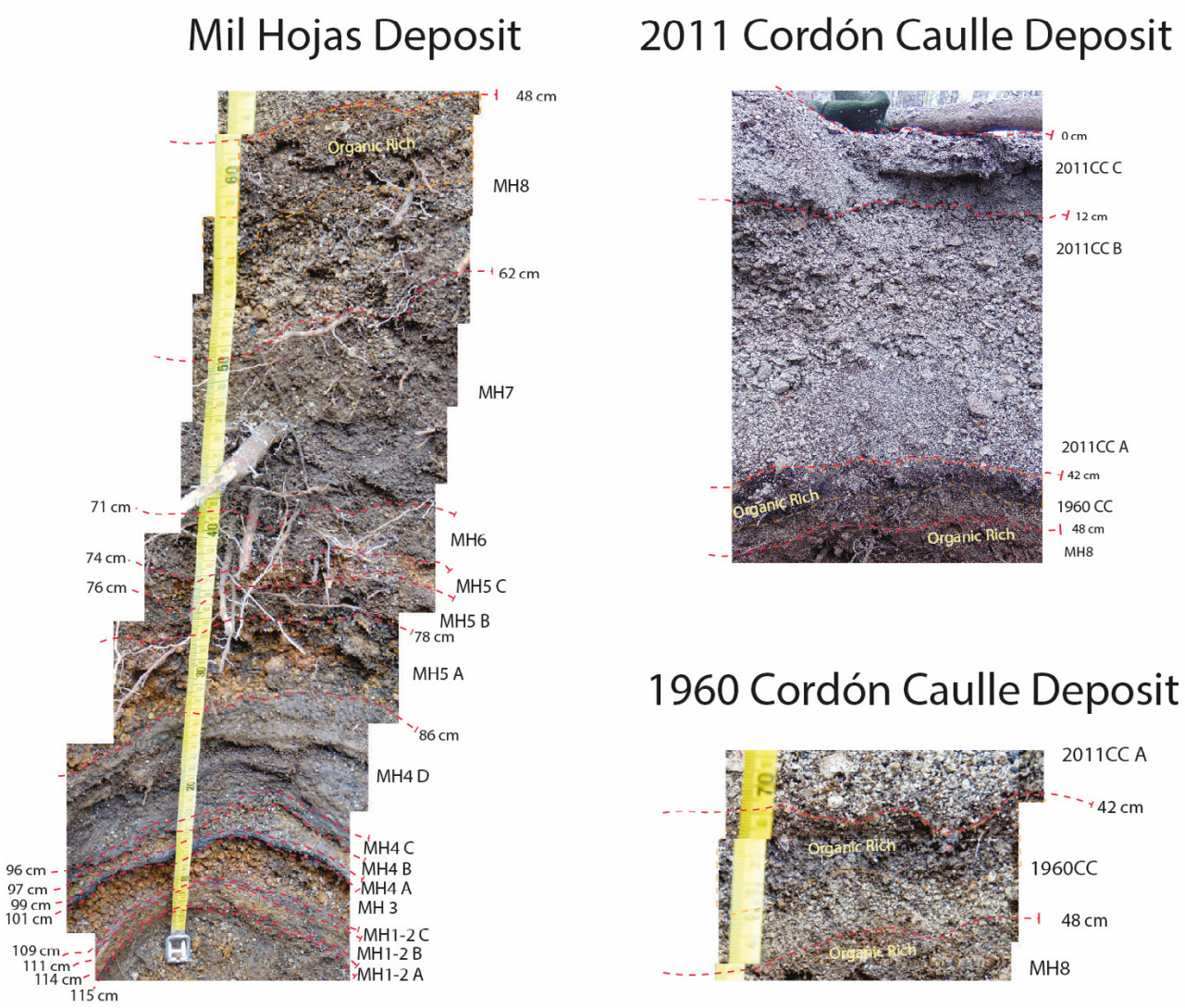


Figure 2: Stratigraphic profile and units identified in the Cardenal Samoré Trial Pit. Left: the Mil Hojas (MH) tephra deposit is observed with its subunits and layer boundaries in red. Bottom-right: the 1960 deposit of Cordón Caulle (1960CC) is visible. Upper-right: the 2011 Cordón Caulle deposit (2011CC). Some incipient organic-rich soil horizons are also noticeable limiting tephra deposits. Depth refers to continuous cm from the surface downwards; deeper boundaries are curved due to the shape of the trial pit.

dispersion for this 1960CC event was reconstructed from historical records [Petit-Breuilh Sepúlveda 2004], the isopach map for this eruption is not available due to the lack of suitable outcrops [Naranjo et al. 2017]. However, historical written reports support that the 1960CC plume was dispersed mainly to the southeast (while the 1921–22 Cordón Caulle eruption was mainly dispersed toward the east-northeast), where the Nahuel Huapi Lake region (Figure 1) was the most affected area [González-Ferrán 1995; Petit-Breuilh Sepúlveda 2004; Naranjo et al. 2017]. This level corresponds to a light grey layer, coarse ash to lapilli grain size, with white pumice, scoria, and crystaloclast as the main components (Figure 3; see Section 3).

The most recent deposit is indicated as a marker horizon originating from the 2011 eruption of the Cordón Caulle fissure system (2011CC; Figure 1). The eruption started on June 4, 2011, lasting approximately until April 2012, although tephra deposits were generated mostly during the first days of the event when the more explosive eruptive phases occurred [Pistolesi et al. 2015]. The resulting stratigraphy of this event is complex and spatially dynamic due to variations in wind direction during the eruptive period. On the eastern slope of the volcanic complex, 13 main tephra levels were described, and grouped into 4 units [Pistolesi et al. 2015]. In the trial pit studied here the granulometric climax of the basal lapillitic pumice graded to upper coarse ash, correlating with the units I and III observed by Pistolesi et al. [2015]. Pyroclastic particles of this unit are very well preserved, with similar characteristics to the products studied by Daga et al. [2014], Pistolesi et al. [2015], and Naranjo et al. [2017]. Although the components in the fraction corresponding to the mode are dominated by pumice (Figure 3), particles like brown glass shards, scoria, obsidians, and crystaloclasts are present, in lower abundance, in the finer grain size fractions (see Section 3).

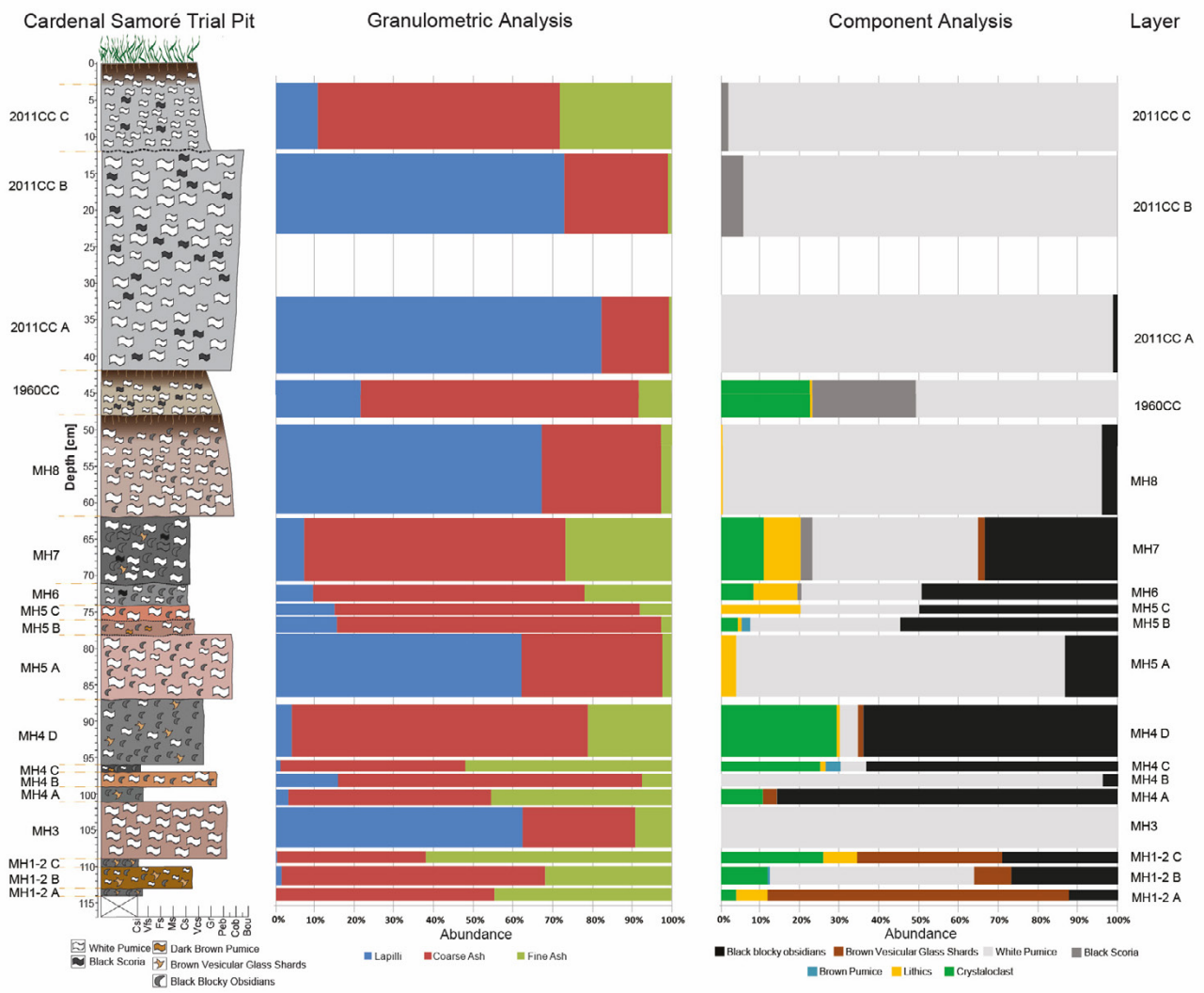


Figure 3: Stratigraphic profile with units and subunits identified in the Cardenal Samoré Trial Pit with grain size and component analyses of the volcanic layers.

## 2 Methodology

### 2.1 Sample collection

We recovered samples of the different subunits of the MH and Cordón Caulle deposits from the trial pit opened 20 km east-southeast from PCCVC (40°43'8"S, 71°56'15"W; Figures 1 and 2) and stored them in labeled bags for further laboratory analysis. We sampled the units and subunits shown in Figure 1, collecting approximately 250–500 g per unit/subunit, depending on the thickness of each one. To support the units and subunits correlations, we described and photographed macroscopic sedimentary features such as boundaries, structure, depth, and number of layers, as well as their coloration, friability, moisture, and presence of macroscopic organic particles.

### 2.2 Grain size

We lyophilized tephra samples and dry-sieved them at one-ϕ intervals ($\phi = -\log_2 D$, where $D$ is the particle diameter in millimeters) using metallic meshes (Supplementary Material 1 Table S1 and Supplementary Material 1 Figure S1). We classified tephras granullometrically as lapilli (−1 to −6ϕ; 2–64 mm), coarse ash (−1 to 4ϕ; 2–1/16 mm), and fine ash (<4ϕ; <1/16 mm) following the nomenclature for pyroclastic sediments [Fisher 1961]; bombs and blocks (>-6ϕ; >64 mm) are not present in the profile.

### 2.3 Macroscopic and microscopic particle descriptions

We carried out optical observations under the binocular magnifying glass for each grain size fraction identifying different types of volcanic particles; i.e. white and dark brown pumice, black scoria fragments, glass shards (vesicular and blocky obsidians), crystaloclasts, and lithics. We conducted componentry analysis on the fraction of mode 1 – or the second coarsest mode when mode 1 corresponded to 4ϕ – of each unit/subunit counting 200–300 particles per level (expressed as percentages relative to the total counted components;Supplementary Material 1 Table S1). We performed the morphological characterization of different representative particle types (mainly from the layers where they more abundant) by a binocular magnifying glass and scanning electron microscope operating at 5 kV (SEM, model FEI Inspect-S50, Department of Materials Characterization – Centro Atómico Bariloche). Also,

we prepared polished resin sections by embedding selected pyroclastic particles (125–2000 µm; 3 to -1ϕ) in epoxy through manual picking under a binocular microscope, and polishing the stubs down after pyroclasts were exposed. These selected particles represent the components of each identified tephra level. We documented the distribution of particles within the stubs through photography before sputter coating to determine their exact locations. Subsequently, we observed these polished sections under SEM operating in backscattered electron (BSE) mode at 20 kV to examine vesicularity, internal texture, mineral phases, abundance of a glassy matrix, and compositional information (see Section 2.4). We used images at several magnifications to ensure the optimum resolution for this analysis [Shea et al. 2010]. We calculated the degree of vesicularity and crystallinity (and different mineral phases) by analysis of scaled high-resolution BSE images, by the open-source image processing software `Fiji ImageJ` [Schindelin et al. 2012]. This required manual image segmentation and partitioning into multiple classes of similar attributes (e.g. pixel color, the shape of the object, etc.) defining the boundaries between vesicles, glass, and immersed crystals/microlites in a particle; the final value of these parameters were obtained by calculating their corresponding areas [Hu et al. 2019]. The estimations provided in this study are based on area percentage (area%) measurements rather than volumetric assessments. Even though the texture of the rocks is a 3-D property, analyzing abundance and size distribution of vesicles and crystals using 2-D analyses (of several particles from similar macroscopic features) is considered a starting point to parametrize textural features, with the purpose to describe clast textures as is frequently used [Visalli et al. 2023; Manzotti et al. 2024; Rojas et al. 2024, among others] rather than to develop process modeling based on such information.

### 2.4 Geochemical characterization

To get extra information to compare with textural analyses, we carried out diverse geochemical measurements. We separated 22 samples (5–50 mg) by picking under a binocular magnifying glass to obtain the bulk rock composition of each of the most representative components. The 22 samples correspond to particles from almost all subunits (except MH6 and MH7 due to measurement issues, and 2011CC as it is the deposit with the most available information). From each unit/subunit, each sample belongs to the same size fraction, and was grouped following the criteria of particle types identified: white and brown pumice, scoria, and glass shards particles (brown glass and obsidians). Such samples were analyzed by Instrumental Neutron Activation Analysis (INAA), measuring major (Al, Fe, Ca, Na, K, Mg, Ti, and Mn) and trace elements (La, Ce, Dy, Nd, Sm, Eu, Tb, Yb, Lu, Sb, As, Ba, Br, Cs, Zn, Co, Cr, Hf, Sc, Sr, Rb, Ta, Th, U, V, and Zr). Analytical errors differ for each element and sample analyzed, since they depend on the nuclear parameters of each element, on the irradiation conditions, and the composition of the sample, varying in most elements from 4 to 12 % and increasing for Sr, Br, Cr, and Zr up to around 20 %. Certified reference materials CRM NIST 2709a San Joaquin Soil and CRM IAEA Soil 7 were analyzed together with the samples for analytical quality control (Supplementary Material 1 Table S2). The analytical methodology is described elsewhere [Daga et al. 2006]. We use trace elements to show the tephra-PCCVC correlation. Also, as measurements from the INAA technique do not report Si concentrations (due to nuclear issues), we converted major elements to oxides, and $SiO_2$ contents were estimated by mass difference to get a comparative estimate between samples (Supplementary Material 1 Table S3).

In addition, we employed an energy-dispersive X-ray analysis (EDS, attached to the SEM) for some detailed compositional information of micron features during the textural analysis on polished sections. Due to the small sizes (microns) of textural features of interest to be analyzed, we chose spot/point measurements at all sites of interest to obtain comparative analyses (under similar measurement conditions: 20 kV, 5 nA current, beam size 5–6 µm, count time of 100 s). Even though this method is considered a semi-quantification of major elements (Si, Al, Fe, Ca, Na, K, Mg, Ti, Mn, and P), it is still helpful when very small areas are analyzed [Iverson et al. 2017] and especially here, to make a comparison between samples measured under the same analytical conditions. In this way, we obtained comparative measurements on glass (Supplementary Material 1 Table S4) and identification of mineral phases which are analyzed together with textural characterization.

## 3 Results

### 3.1 Granulometry and componentry of tephra layers

The grain size distribution in the different tephra layers shows variations between MH, 1960CC, and 2011CC; notable differences are also observed within each of the multilayer deposits of MH and 2011CC, varying from fine ash to lapilli (Figure 3). Componentry analysis reveals that white pumices are a common pyroclast, albeit in varying proportions, across all three main deposits. On the other hand, brown vesicular glass shards and brown pumices were only found in MH, along with a higher presence of lithics, crystal fragments, and scoria (Figure 3; Supplementary Material 1 Table S1). As previously defined, MH is composed of alternating dark fine and beige coarse layers limiting eight subunits [Naranjo et al. 2017]. Even with internal layering, MH1-2, MH4, and MH6 are the subunits with a higher abundance of dark components. These subunits stand out by the dark coarse ash size layers due to high abundance of black blocky obsidians and brown vesicular glass shards (the sum of these components reaches 66–88 % in MH1-2 A, C; 63–89 % in MH4 A, C, D; and 49 % in MH6) intercalated with coarse ash to lapillitic beige layers, with high abundance of white pumice (51 % in MH1-2 B and 96 % in MH4 B; Figure 3). Crystaloclasts and lithics are the least abundant components, but represent up to 30 % of the dark fine levels. In MH7 dark (obsidians) and light (pumices) components are similar (33 % vs. 41 %, respectively; Figure 3). On the other hand, thicker lapillitic beige layers are conformed by MH3, MH5 (with dark fine intercalations), and MH8, with high abundance of pumice reaching 82–100 % of the number of components (Figure 3). In the other grain size fractions, the proportion of components vary, usually with high abundance

of white pumice in the coarse fractions, while obsidian, lithics, and crystals are dominant in the finer fractions.

On the other hand, the Cordón Caulle tephras are predominantly composed of coarse ash to lapillitic white pumice in the fraction corresponding to the mode. Specifically, the mode of the 1960CC deposit consists of 50 % white pumice along with smaller proportions of black scoria (26 %) and crystaloclasts (22 %; Figure 3). In contrast, the mode of 2011CC deposit is dominantly composed of lapilli-sized white pumice (>93 %), with minimal presence of black scoria (<6 %). The upper part of the 2011CC deposit shows a decrease in grain size but it is still dominated by white pumice particles (Figure 3). While the componentry of the mode fraction in CC deposits differs from that of the MH deposit, the same components that were observed in MH are identified in fractions finer than the mode in CC tephras.

### 3.2 Texture/microtexture characterization of tephra components

We classified particles according to: (1) the morphological features as the first character that is observed (under magnifying glass), and (2) the groundmass microtexture (under SEM), varying even within similar morphological types. The groundmass (comparative) composition and mineralogy are also considered in the description of each subtype of particle to highlight differences among them.

#### 3.2.1 *White pumice*

White pumice (*WP*; Figure 4A) is the most abundant particle in granulometric modes of MH beige subunits and CC tephras; also it is a common component in grain size fractions >250 µm from all subunits. In MH, the pumice color varies from white (MH8) to yellowish (MH1-2; Figure 2), with broken fragments retaining the white cores. The vesiculation degree of *WP* reaches 68–86 area%, with two different arrangements, elongated and massive vesicles. The particle morphologies reflect these characteristics. Fragments with dominance of tube-like vesicles are elongated, and have a fibrous aspect and silky-vitreous luster (Figure 4B and 4C). Vesicles can be parallel to each other, as well as curved by sectors defining convoluted arrangements (Figure 4D and 4E). On the other hand, those with subspherical to irregular vesicles without preferential orientation or spongy-like, have irregular to subequant shapes, with saccharoid aspect and vitreous luster (Figure 4F–4H). Vesicle diameters range from 15–125 µm in both types.

Corroded surfaces with recrystallization have been observed in some particles (Figure 5), mainly at the base of the sequence. The edges of vesicles are semi-circular in some cases and very irregular and discontinuous in others (Figure 5). Apparent ring-shaped and flake-shaped recrystallization protrusions could be identified on the walls of some volcanic glass particles resembling clay formation (Figure 5). From this, it could be inferred that the yellowish color observed in *WP* from MH indicates weathering processes.

*WP* are aphyric to porphyric (Figure 6), with immersed plagioclase (Figure 6A, 6B, and 6D), pyroxene (>250 µm), Fe-Ti oxides, and apatite (as inclusions commonly <50 µm), forming glomerocrysts (Figure 6C and 6D). In elongated pumices immersed crystals are rare; parallel and convoluted vesicles of well-preserved glass are common (Figure 6E–6F). The groundmass glass has a narrow range of $SiO_2$ composition varying between 69–72 wt.% ($n$ = 10 particles). MH and CC pumices are not differentiated by the $SiO_2$ content, however, at the grain size analyzed, phenocrysts/glomerocrysts with reabsorbed boundaries embedded in the glassy matrix seem to be more abundant and larger in MH than CC.

#### 3.2.2 *Dark brown pumice*

Dark brown pumice (*BP*) fragments are present particularly in the granulometric mode of MH4 C and MH5 B (4 % and 2 % of the total components, respectively) subunits; although *BP* is not present in all mode fractions (Figure 3), they are also identified in coarser fractions of the other MH and CC levels. In general, they have subrounded shapes and smaller grain size and lower degree of vesicularity (30–50 area% in MH, and reaching up to 65 area% in CC) than *WP* fragments. *BP* fragments have mainly spherical to subspherical vesicles, thus dark brown pumices with spongy, saccharoid, and subequant macroscopic shapes are identified (Figure 7). In some cases, vesicles shapes coalesce giving irregular forms. Although they showed a similar petrology to *WP*, the microtexture of *BP* showed different features, classifying in two types in both MH and CC tephras. In this case, groundmass glass composition differs between MH (~54–59 wt.% $SiO_2$) and CC (~61–69 wt.% $SiO_2$), independent of the textural type ($n$ = 6 particles).

Type *BP1* was defined in very low proportion, with only one particle found at MH and another at CC, among all *BP* analyzed. Despite its rarity, *BP1* is characterized by fresh glass in the groundmass, moderate vesicularity (25–38 area%), and porphyritic texture with approximately 28 area% of crystallinity. The phenocrysts are commonly zoned plagioclase, appearing as euhedral tabular phenocrysts (~300 µm in size). The groundmass consists of glass and microlite (less than ~100 µm) crystals composed of prismatic and skeletal plagioclase (~40 µm), few subhedral and very small Fe-Ti oxides (<40 µm) in the border of phenocrysts, and also immersed in the well preserved glassy matrix (Figure 7D–7F).

On the other hand, the type *BP2* exhibits more abundance of microlites distributed homogenously in the groundmass or as patches, with a higher degree of vesicularity, ranging from 30–63 area%. Vesicles are irregular, from subspherical (Figure 7G) to flattened and bent in some sectors (Figure 7J), with a wide range of sizes (20–200 µm). Microporphyritic textures are the result of the high amount of microlites in some cases. Groundmass in some *BP2* particles consists of microlite crystals reaching 75 area% of the matrix area fraction, with almost absence of interstitial glass or full of nanolites. The abundant acicular and swallow-tailed microlites (>40 µm) of plagioclase and pyroxene, and very fine minerals (<5 µm, possibly Fe-Ti oxides), make the identification of glassy matrix difficult in some cases (Figure 7H and 7I). Spherulitic textures with plagioclase and pyroxene microlites are also identified. Some of these particles show microtextural patches or bands of microlite/nanolites (of similar composition to those previously mentioned), as zonal alteration or recrystallization zones, with very

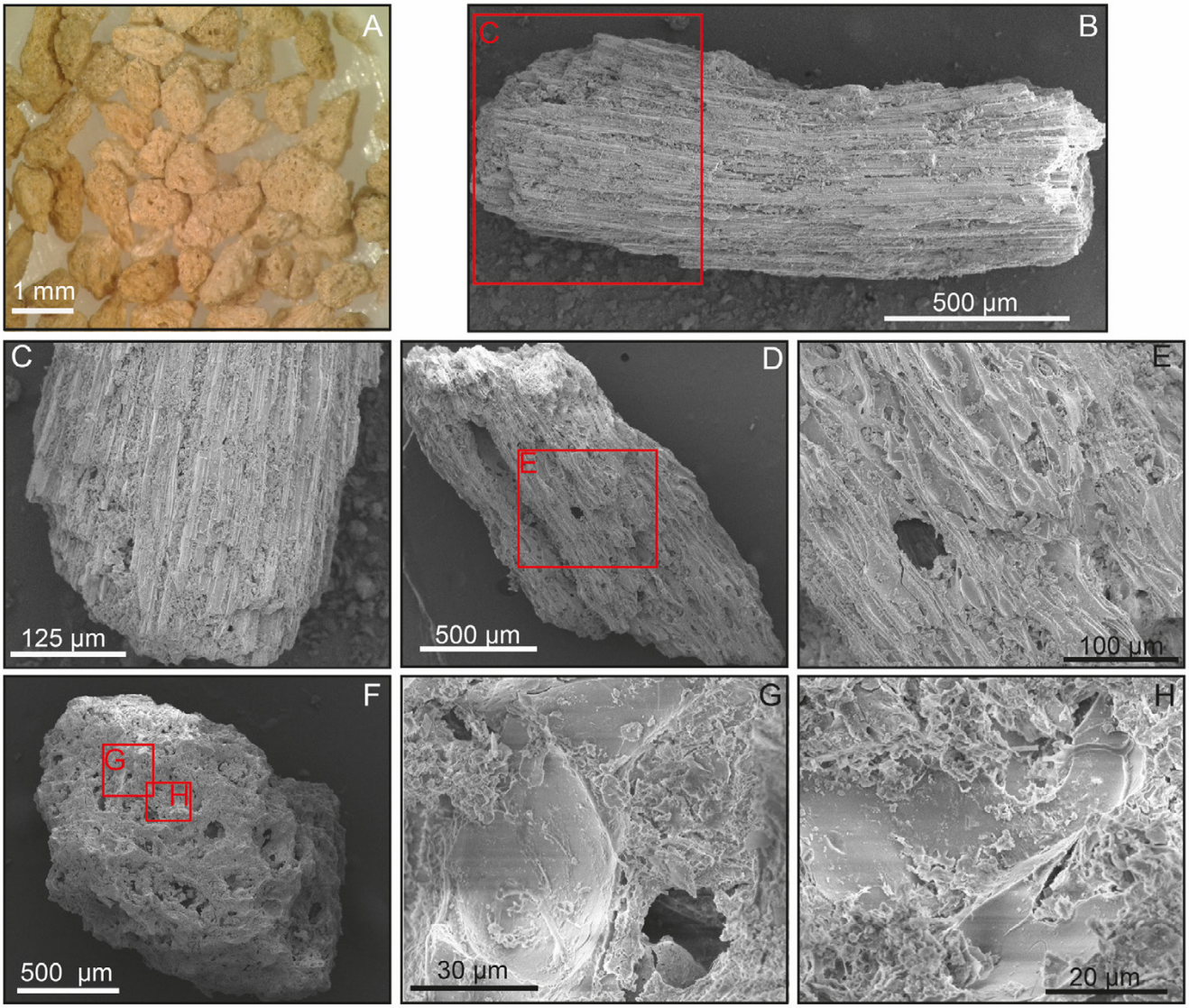


Figure 4: Morphology of white pumice. [A] White pumice of different morphologies under binocular magnifying glass. [B] Elongated or tube-like pumice with parallel vesicles (MH5C). [C] Magnification of parallel vesiculation of B. [D] Elongated white pumice with convoluted vesiculation (1960CC). [E] Magnification of vesicular arrangements of E. [F] Saccharoid or spongy-like pumice (MH5C). [G] and [H] Volcanic glass vesicle with soft surfaces and zones with corroded features, magnifications from F. [B]–[H] are SEM images.

tight flattened vesicles and aligned spherulitic shapes (Figure 7K and 7L).

### 3.2.3 *Scoria*

Scoria (*Sa*) particles are mainly identified in CC tephras (more abundant in the 125–500 µm but can reach up to 2–3 mm size) while are less abundant in MH (all grain size fractions). The MH deposit exhibits scoria particles only in the grain size mode of MH6 and MH7, with less than 3 % of the amount of components. Conversely, the highest percentage of *Sa* particles is in 1960CC, with 26 %, while 2011CC has less than 6 % (2011CC B and C) of *Sa* from the total components (Figure 3). Scoria particles are dark grey to black (Figure 8A.). In general, all the scoria fragments have a macroscopic saccharoid subequant feature, without any preferential vesicular orientation (Figure 8B and 8C). However, despite their similar coloration and macroscopic shape, two internal textural types were differentiated, both with variable degrees of vesicularity.

Type *Sa1* particles are differentiated by a nearly aphyric groundmass (Figure 8D) to porphyritic (with low content, <1 area%, of relatively small phenocrysts; Figure 8E and 8F) texture, with highly variable degree of vesicularity (10–70 area%). The shapes of the vesicles are irregular, with <70 µm size, and usually show incipient convoluted arrangements by sectors. Subhedral to anhedral plagioclase, pyroxene, and Fe-Ti oxide phenocrysts >100 µm can be found in a well-preserved glass matrix. The glassy groundmass showed a restricted composition between 68–71 wt.% $SiO_2$ ($n$ = 5 particles).

Type *Sa2*, on the contrary, exhibits clear microporphyritic textures. These particles have less vesicularity than the *Sa1* type but also vary between 5–50 area%,

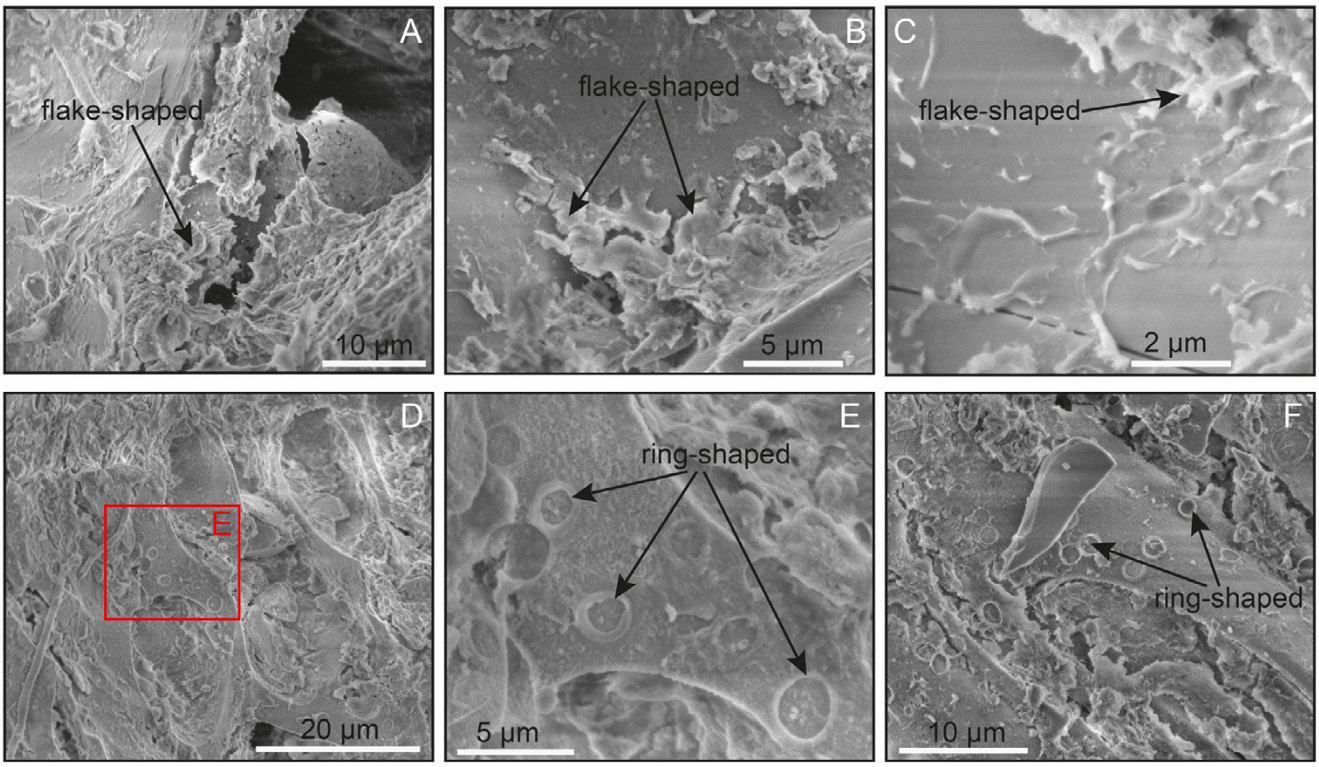


Figure 5: SEM images of different alteration features in surfaces of pumice for [A]–[C] MH5C and [D]–[F] MH4B.

with well-preserved subspherical-shaped vesicles between a few microns to >80 µm (Figure 8G). The groundmass consists of variable amounts of microlites (5–45 area%) with interstitial glass in some particles (Figure 8H), while the interstitial space is occupied by nanolites forming patches in others (Figure 8I). The microporphyritic textures result from mainly euhedral tabular plagioclase (<80 µm), small swallow-tailed and rhombic/skeletal-shaped pyroxenes (<15 µm), and Fe-Ti oxide and apatite (<10 µm; Figure 8H). These particles showed zonal recrystallization textures or undercooling/supersaturation conditions in the matrix and also at the borders of phenocrysts (mainly plagioclase). Some mineral phases (<10 µm) with acicular habit can be found isolated without preferential orientation or in contact with each other with radiating arrays of acicular crystals, like spherulitic textures (Figure 8I). In this *Sa2* type, the glassy groundmass exhibits a wide compositional range (54–73 wt.% $SiO_2$; $n$ = 9 particles).

### 3.2.4 *Glass shards*

The next subdivision examines the sizes and shapes of glass shards, providing insights derived from macroscopic observations. This comprehensive analysis aims to elucidate the characteristics and variations present within the observed glassy fragments, primarily focusing on their coloration.

*Brown glass shards.* The group corresponding to brown glass shards (*GS*) exhibits a brown color of glass varying in shapes from low vesicularity, cuspate, and blocky shards (Figure 9). *GS* are abundant in granulometric modes of MH1-2 subunits varying between 9–75 % of the total mode components. In the other MH levels, *GS* usually comprises the <500 µm fraction, but can reach up to 2 mm in size. The glassy fragments are dark to pale brown, depending on the size and thickness of the particles, with intense vitreous luster (Figure 9A). Spherical to subspherical vesicles between 50 and 200 µm are common in particles with low vesicularity (<5 area%); some of these particles show smooth, fluid-shaped glassy surfaces (Figure 9B and C). Blocky shards are dense fragments with cuspate edges and smooth surfaces. Although groundmass composition is similar (66–71 wt.% $SiO_2$; $n$ = 6 particles), two types of microtextures were observed:

Type *GS1* particles are brown, nearly aphyric, with glassy groundmass and rare apatite (Figure 9D and 9E). Generally, the crystals are anhedral, with textures embedded and reabsorbed by the glass. In polished sections, the vesicles are semicircular and elongated, with diameters between 20–200 µm (Figure 9E and 9F).

Type *GS2* fragments exhibit pale to dark brown macroscopic banding with net limits (Figure 9G), as observed in their microtexture. They show a porphyritic texture, containing subhedral to anhedral plagioclase (>350 µm), pyroxene and Fe-Ti oxides (<200 µm), and Fe-Cu sulfides (<20 µm; Figure 9H, 9I, and 9K), varying between 2–25 area%. Embedded and reabsorbed textures in phenocryst mineral phases can also be found in plagioclase, pyroxene, and Fe-Ti Oxides (Figure 9K). The groundmass showed microtexture differences between pale and dark brown bands. Pale brown bands correspond mostly to microlite-free matrix, with patches of plagioclase/oxides microlites/nanolites. Conversely, the groundmass of darker bands comprises numerous mineral phases <5 µm, or nanolites, consisting predominantly of plagioclase; spherulitic pyroxene and oxides may also be present (due

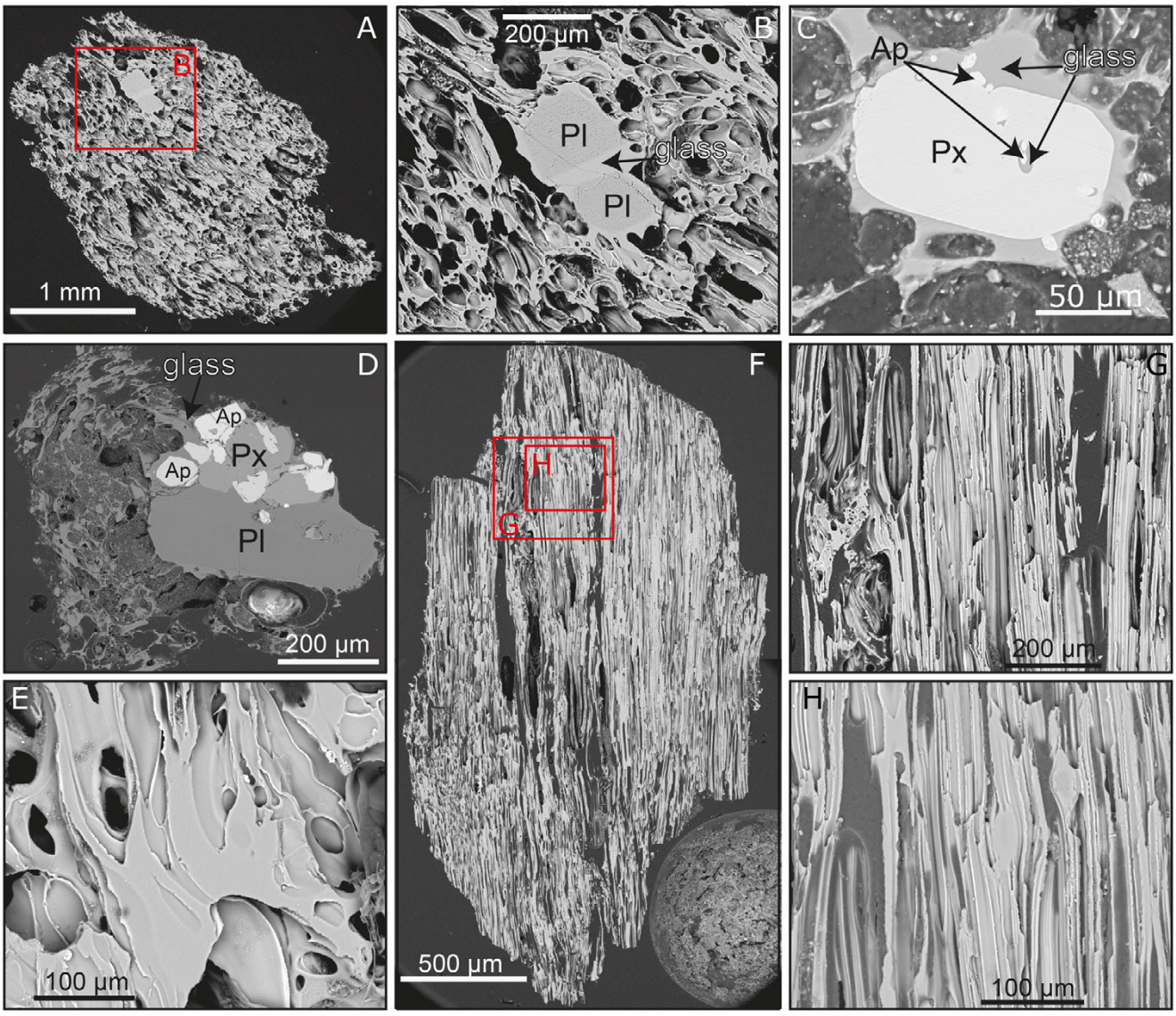


Figure 6: BSE images of polished sections of white pumice. [A] and [B] Spongy-like pumice with subhedral plagioclase (Pl) phenocrysts (MH8). [C] Subhedral pyroxene (Px) with apatite (Ap) and glass inclusions surrounded by a vesicular glass coating (MH4B). [D] Spongy-like pumice with glomerocryst of subhedral plagioclase (Pl), pyroxene (Px), and small apatite (Ap) (MH5A). [E] Curved vesiculation arrangement in aphyric volcanic glass (N layer). [F] Aphyric pumice with fluidal vesicles (1960CC). [G] and [H] Elongated and tortuous vesicles, magnifications of F.

to the small size of these two phases, their individualization and recognition were difficult). These mineral bands exhibit repetitive nanometric to micrometric bandings, with minimal interstitial glass presence (Figure 9H–9L). These mineral bands are usually deflected around crystals and vesicles, defining flow textures.

*Blocky obsidian.* The obsidians (*Ob*) are black blocky glassy fragments with vitreous luster, soft faces, and absent of vesicles. They are abundant in the column, mainly in dark-fine layers from MH subunits, and are also generally found composing the fraction between 125–500 µm, although reaching up to 1 mm size both in MH and CC layers (Figure 10A). Cuspidal forms of concave-convex edges are generated by conchoidal fractures (Figure 10B and 10C). Textural types identified in these particles, *Ob1* and *Ob2*, are similar to those described for vesicular glass shards, and both type of particles can be distinguished only by macroscopic color. Thus, *Ob1* corresponds to aphyric particles, with scarce anhedral apatite <50 µm (Figure 10D–10F), while *Ob2* corresponds to particles exhibiting porphyritic banded textures (Figure 10G–10L), with subhedral pyroxenes, plagioclase, and Fe-Ti oxides >250 µm. These *Ob2* particles display repetitive banded textures with a groundmass composed of microlite/nanolite pyroxene/oxides and interstitial glass (Figure 10I, K, and L). The banded textures of the *Ob2* particles exhibited no noticeable variations in $SiO_2$ content of the glass across the individual bands within the same particle. The composition of groundmass glass varies (68–74 wt.% $SiO_2$; $n$ = 9 particles) not allowing to discriminate between *Ob1* or *Ob2* types (Supplementary Material 1 Table S4).

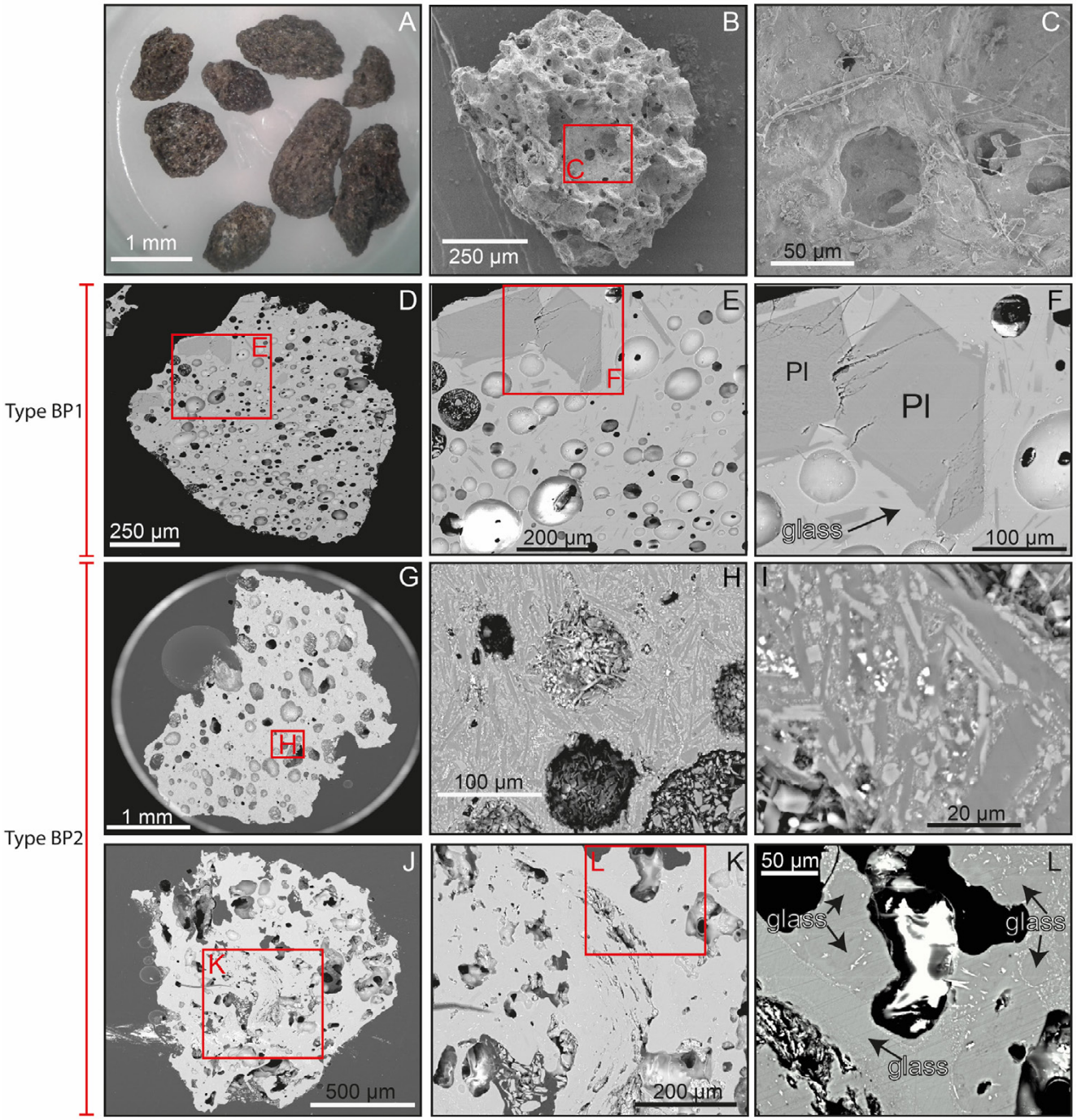


Figure 7: [A] Brown pumice morphologies. [B] Saccharoid-like brown pumice (MH8). [C] Semicircular vesicles, magnification of B. [D]–[F] Brown pumice *BP1* textural type (MH8): porphyritic texture with plagioclase (Pl) crystals and small plagioclase microlites in a well preserved glass with spherical to subspherical vesicles. [G] and [J] Brown pumice *BP2* textural type (MH8 and 1960CC, respectively). [H] and [I] Irregular vesicles and microporphyritic texture without glassy matrix, magnifications of G. [K] and [L] Irregular and flattened vesicles with zoned acicular microporphyritic textures, magnifications of J. [A] Binocular magnifying glass image; [B]–[C] SEM images; and [D]–[L] BSE images.

*Crystaloclasts.* Crystals and crystal fragments (*Cr*) are found in all tephra levels in <2000 µm fractions. Their abundance in granulometric modes varies between 4–29 % of the total components (Figure 3). The MH deposit exhibited variation in the abundance of crystals in the modes of subunits where are present, exceeding 20 % of the total components for MH1-2 C, MH5C, and MH5D modes (Figure 3). Similarly, the 1960CC deposit showed 22 % crystal abundance (Figure 3). In all cases they are coated by glass, generating glassy luster and vesicular surface textures in the particles (Figure 11A and 11B). Even if they are coated with glass, it is possible to observe the shape and color of the crystals, evident in binocular magnifying glass (Figure 11C and 11E). The most abundant phase corresponds to white euhedral to subhedral tabular pla-

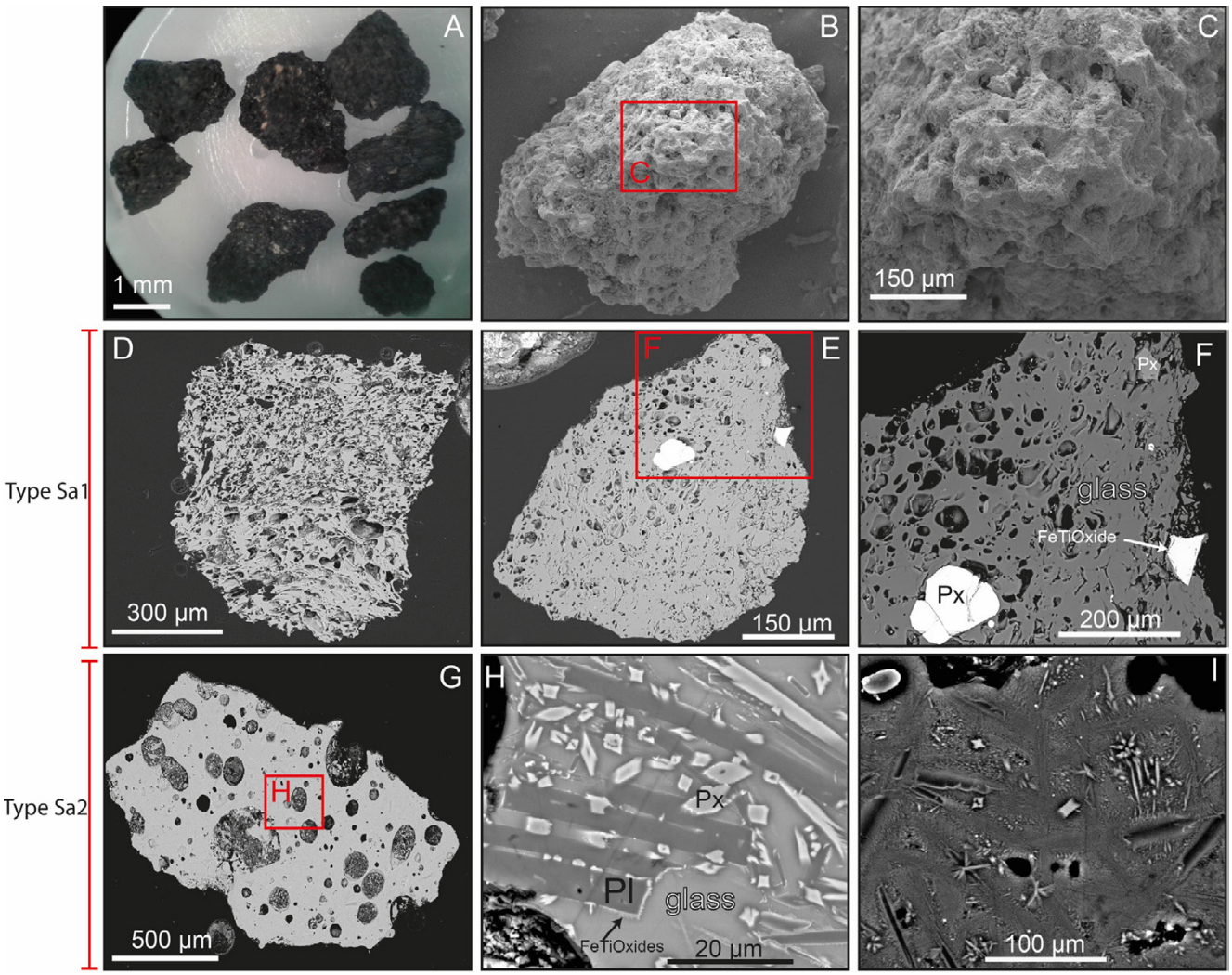


Figure 8: [A] Black scoria morphologies. [B] Saccharoid-like black scoria (MH8). [C] Subrounded surfaces and irregular vesicles, magnification of B. [D] Aphyric scoria *Sa1* type (MH8). [E] Porphyric scoria *Sa1* type with pyroxene (Px) and Fe-Ti oxide immersed in a well preserved glass (MH5A). [G] and [H] Scoria *Sa2* type of subspherical vesiculation, with euhedral plagioclase and pyroxene phenocrysts with very small Fe-Ti oxides growing in contact (MH8). [I] Recrystallization textures with very fine microlites and spherulites in glassy matrix (1960CC). [A] Binocular magnifying glass image; [B]–[C] SEM images; and [D]–[I] BSE images.

gioclase crystals between 50 and 1250 µm. Plagioclase fragments with anhedral inclusions of Fe-Ti oxides <30 µm are less abundant (Figure 11C and 11D). Prismatic and subhedral green and brown pyroxene crystals between 50 and 200 µm are also frequent with a large number of inclusions (<50 µm) of glass and subhedral apatite and Fe-Ti oxides (Figure 11E and 11F).

### 3.3 Bulk geochemistry of pyroclastic fragments

The geochemical data obtained for the different kinds of selected particles according to optical features is presented in Figure 12 andSupplementary Material 1 Table S3. Bulk major and trace elements were determined on 22 samples: 9 *WP*, 2 *BP*, 3 *GS*, 7 *Ob*, and 1 *Sa*. In Figure 12, the bulk chemical composition of post-glacial PCCVC caldera units and tephra fall out from previous studies [Gerlach et al. 1988; Singer et al. 2008; Pistolesi et al. 2015; Naranjo et al. 2017] is presented for comparison purposes in addition to the data obtained in this study.

All samples are enriched with respect to the primitive mantle proposed by McDonough and Sun [1995]. In general, a greater enrichment of the large ion lithophile elements (LILE) is observed with respect to those of high field strength elements (HFSE). Similarly, there is greater enrichment in light (LREE) than in heavy rare earth elements (HREE). Also, this geochemical fingerprint is characterized by strong negative anomalies in Ta, Sr, and Ti. A negative Eu anomaly can be observed in the REE. Although the pattern shape is similar for all samples, one brown pumice sample from the 1960CC layer [*BP*(1960CC)] and one scoria sample from the MH8 layer [*Sa*(MH8)] show a lower enrichment pattern regarding the other samples, with minor Sr and Ti anomalies (Figure 12)

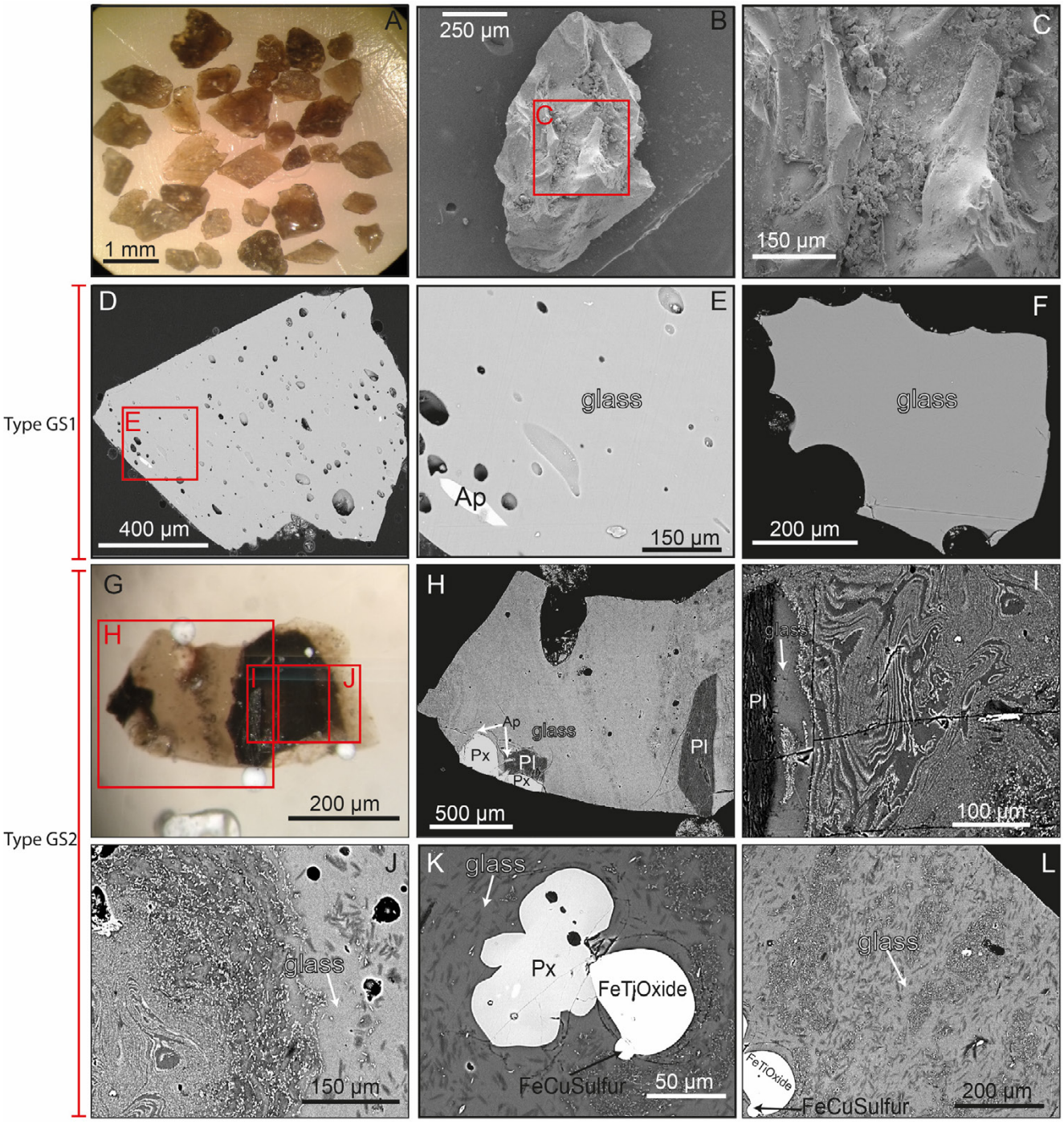


Figure 9: [A] Vesicular glass shard morphologies. [B] Vesicular glass shard (MH3). [C] Soft glass surfaces with fine aggregates, magnification of B. [D] and [E] Nearly aphyric glass shard *GS1* type of low vesiculation with anhedral apatite (Ap) immersed (MH5B). [F] Aphyric glass shard *GS1* type (MH1-2B). [G] Vesicular glass shard *GS2* type with alternation of dark and light brown bands (MH8). [H] Detail of contact between light (microlite-free) and dark brown (microporphyritic) glass; glomerocryst of subhedral plagioclase (Pl), pyroxene (Px), and apatite immersed (left) and subhedral plagioclase phenocryst in contact with different anastomosed glass bands (right), magnification of G. [I] Detail of the dark brown glass; white bands are formed by micrometric crystals marking flow textures, magnification of G. [J–L] *GS2* type glass shards with anhedral phenocrysts of pyroxenes, Fe-Ti oxide, and Fe-Cu sulfides immersed in glass bands; these bands are formed by zones of rich and poor micrometric mineral growth (MH8). [A] and [G] Binocular magnifying glass image; [B] and [C] SEM images; and [D]–[F] and [H]–[L] BSE images.

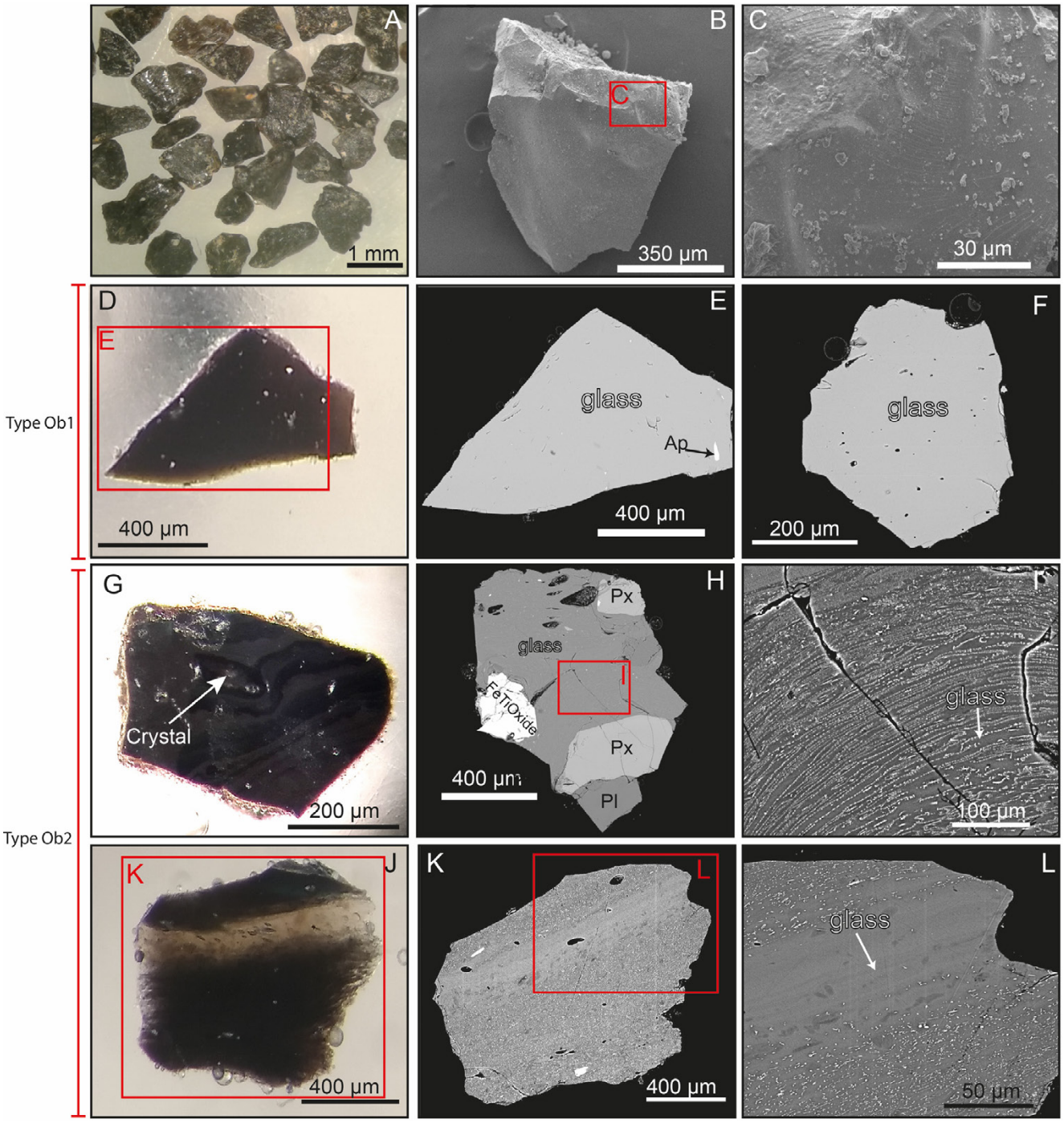


Figure 10: [A] Blocky obsidian morphologies. [B] Blocky obsidians (1960CC). [C] Blocky obsidian of null vesiculation, with soft glass surfaces and conchoidal fractures, magnification of B. [D] and [E] Nearly aphyric angular blocky obsidian *Ob1* type with anhedral apatite (Ap) immersed in a well preserved glass (MH1-2B). [F] Low vesicularity aphyric obsidian *Ob1* type (MH3). [G] *Ob2* type with alternation color banding (note that the band surround a crystal in the middle of the particle; (MH1-2c). [H] and [I] Porphyritic obsidian *Ob2* type of low vesicularity with subhedral to anhedral plagioclase (Pl), pyroxene (Px), and Fe-Ti oxide in contact with different crystal-rich and crystal-poor micrometric banding (MH5 A). [J] and [K] *Ob2* type with light and dark brown glass, and very thin elongated vesicles (1960CC). [L] Detail of light (nearly aphyric) and dark (microporphyritic) bands; the last one is formed by micrometric crystal rich zones, magnification of K. [A], [D], and [G] Binocular magnifying glass image; [B] and [C] SEM images; and [E], [F], [H], [I], [K], and [L] BSE images.

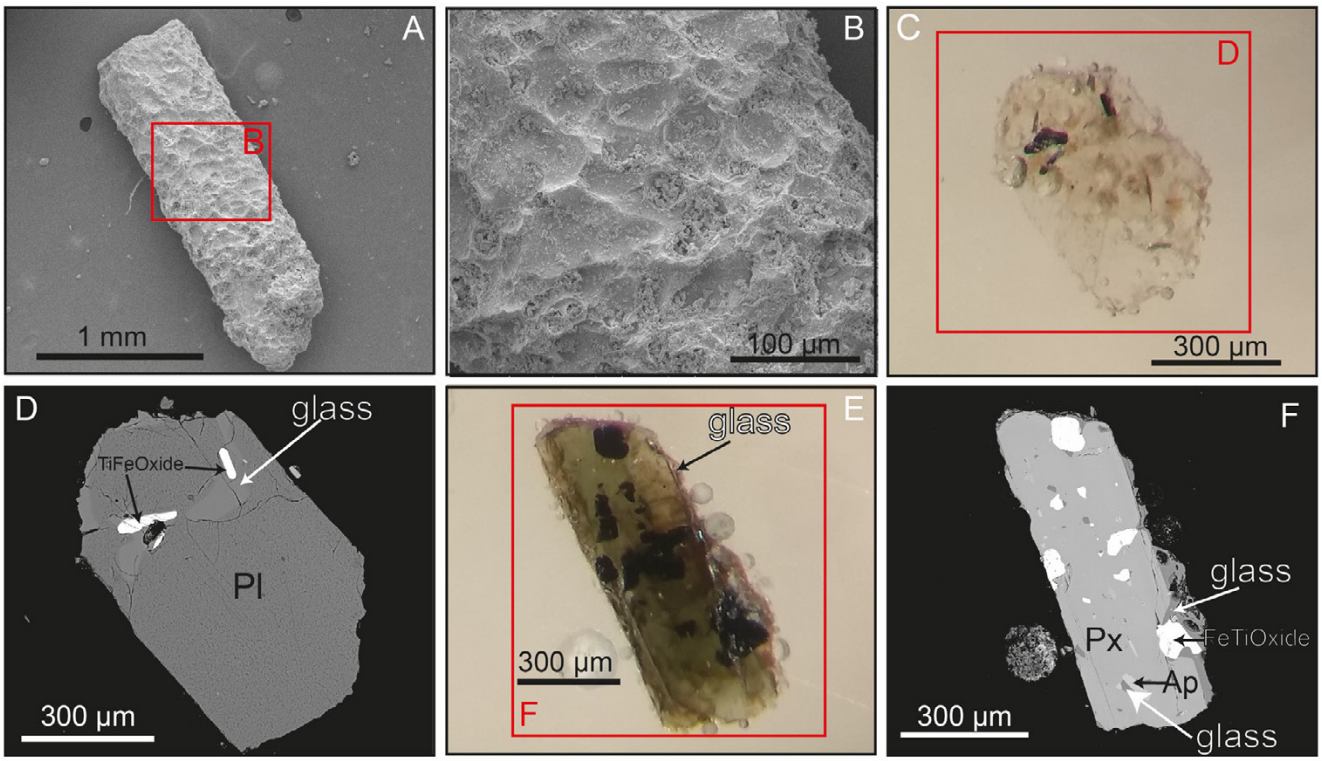


Figure 11: [A] Subhedral prismatic crystal surrounded of volcanic glass (MH5C). [B] Volcanic glass coating surface, magnification of A. [C] and [D] Subhedral plagioclase (Pl) crystaloclast with mineral inclusions of Fe-Ti oxides and glass (MH5C). [E] and [F] Green subhedral pyroxene (Px) coated by glass, with a large number of anhedral inclusions of apatite (Ap), Fe-Ti oxides, and glass (MH5C). [A] and [B] SEM Images; [C] and [E] binocular magnifying glass images; and [D] and [F] BSE images.

(these two kinds of particles are absent from the granulometric modes of these layers, but are found in finer fractions). Despite this difference, the whole pattern closely resembled that known for the PCCVC (Figure 12).

## 4 Discussion

### 4.1 Morphology, texture, and geochemistry defining the origin of particles

Understanding the origin of the components included in a tephra deposit provides unique information, but distinguishing between the different types of particles is not a simple task [Benet et al. 2021]. The analyses of morphological and textural characteristics of the volcanic fragments allow a more detailed evaluation of the processes affecting the volcanic components to explain their juvenile – or not – character, providing information for further correlations and volcanic processes involved.

#### 4.1.1 *Types of juvenile components*

*White pumice.* These particles are the main juvenile component from silicic explosive eruptions. Variations in gas release conditions and physical gradients in the ascending viscous magma lead to variable vesicle distributions and high degrees of vesicularity (>70 %) in white pumice deposited within the same level [Cioni et al. 2015]. The relative rates of bubble nucleation, expansion, and magma ascending play a pivotal role in shaping the textures of primary vesicles [Shea et al. 2010]. Spherical vesicles typically form when magma degasses relatively slow, allowing gas bubbles to expand uniformly in all directions under slow ascent rates. Conversely, elongated vesicles tend to form in more viscous magmas or during rapid explosive fragmentation processes. In these cases, gas bubbles

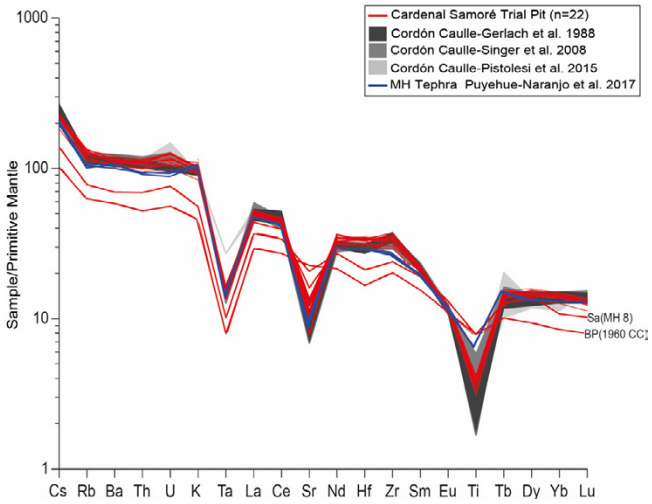


Figure 12: Multi-element diagram normalized to primitive mantle [McDonough and Sun 1995] of different pyroclastic types of Cardenal Samoré tephra deposits and post glacial products from PCCVC [Gerlach et al. 1988; Singer et al. 2008; Pistolesi et al. 2015; Naranjo et al. 2017]. *Sa*(MH8): scoria from MH8; and *BP*(1960CC): brown pumice of 1960CC.

may elongate in a particular direction due to shearing forces or deformation during fragmentation, such as near conduit zones, resulting in elongated or tortuous shapes, influencing the magma permeability [Polacci et al. 2003; Cioni et al. 2015]. Studies on the 2011CC eruption have already indicated that the variability in vesicularity of white pumice is associated with heterogeneities within the magmatic column, induced by differential rates of magma ascent, resulting in stress zoning and variable degassing efficiency [Schipper et al. 2013; Pistolesi et al. 2015]. Despite variations in formation mechanisms, the prevalence of highly vesicular pumice throughout the sedimentary column suggests the significant role of gas exsolution in the latest eruptive events of the PCCVC, reflecting the nature of the eruptions [Rotella et al. 2014].

*Glass shards.* Despite macroscopic differences, both brown glass shards and blocky obsidians exhibited similar particle typologies and internal textures both in MH and CC tephras. The different colors could be associated with variations in grain size within the layer; i.e. light transparent brown fragments are finer than black blocky obsidians, but related to common parental magmas/processes. In CC layers, for example, *Ob* fragments are more abundant than *GS* and is possibly related to the size of the particles observed. Individual fragments of *GS* and *Ob* showed homogeneous composition (>66 wt.% $SiO_2$;Supplementary Material 1 Table S4), while textural features are variable. Both, *GS1* and *Ob1* particles show low crystallinity and well-preserved glassy matrix, suggesting juvenile origin; also, resorption textures and embedded Px and Pl crystals indicate changes in the physical-chemical conditions of a crystal-poor magma.

On the other hand, textures of *GS2* and *Ob2* particles suggest a more complex crystallization history, forming phenocrysts firstly in the magma chamber, and afterward a finer microcrystalline groundmass, possibly during the eruptive processes. Commonly, anastomosed and banded textures may first suggest magma mixing; however, in this case, the analyzed particles present a narrow ranged differences in the chemistry of their glasses (69–73 wt.% $SiO_2$;Supplementary Material 1 Table S4). In some cases, magma quenching includes a short period of quick crystallization, with crystals aligned parallel to flow directions at the time of melt solidification [McPhie 1993]. Magmatic flow can also be determined by changes in color, the orientation of microcrysts in the groundmass, and the selective concentration of crystals, microlites, espherulites or devitrification minerals [González 2008]. In this work, banded textures produce the color banding observed under magnifying glass (Figure 9G and 9J). At other scales, macroscopic banding observed in glassy pumices and bombs from the 2011 Cordón Caulle eruption was attributed to variations in the iron oxidation state, instead of mineralogical or textural features [Castro et al. 2013]. In this study, however, we identify microscopic incipient nucleation and alignment of new mineral phases, generating the flow banding textures. The phases typically exhibit dimensions <5 µm, rendering measurement challenging (some analyses suggest elevated Fe content, possibly corresponding to Fe-oxides (Figure 9I–9L and Figure 10I and 10L). Within these color bands, crystal nucleation and growth processes could be inferred owing to the prevalence of small nanometric crystals alongside micrometric ones. Experimental results have shown both processes, relating color changes in rhyolitic obsidians to changes in the state of iron oxidation and consequent oxide nucleation [Moriizumi et al. 2009]. Another type of *GS2* and *Ob2* particles, furthermore, showed patchy-textures with zones of microlite-rich and microlite-poor glassy groundmass and aligned oxides, as a result of differential mineral recrystallization due possibly to reheating processes [Deardorff and Cashman 2017]. Even though such processes have been experimentally studied for less evolved $SiO_2$ compositions [Deardorff and Cashman 2017], the textures are comparable to the samples under study here.

The variety of glass shard types, mainly obsidians, within a single layer were correlated with the released gases and the rheological evolution of the melt within the same eruptive event [Rust and Cashman 2007; Paisley et al. 2019]. These authors related changes in axial bubble relationships (i.e. spherical vs. elongated shapes), to variations in shear rates and stresses, and proposed changes in the rate of magma rise, position, and conduit obstruction to explain the different obsidians, considering the particles as juvenile [Rust and Cashman 2007]. However, obsidian fragments were attributed to lithic material in the previous description of MH subunits, as one common and characteristic component of the phreatomagmatic layers that helps in the identification of the subunits, while the same kind of particles were considered as juvenile fragments for the 2011 Cordón Caulle eruption in same work [Naranjo et al. 2017]. Also, for the 2011 Cordón Caulle event, other authors identified black, with a weak color banding, to transparent brown clasts as obsidian, associating lighter clasts to possible juvenile material while darker ones can represent accidental lithics from ancient obsidian bodies [Pistolesi et al. 2015]. This last hypothesis is probable in a volcanic complex where pyroclastic deposits and rhyolitic obsidian lava flows are common.

However, we identified here that the color of the fragments is probably not directly associated with the character of the particles; actually, the clear identification of the juvenile or not-juvenile origin of the particles is not an easy task, and both MH and Cordón Caulle glass shards showed the same features. Remarkably, these kinds of textures were recently described for the explosive products from the 2011 Cordón Caulle eruption. In such cases, textural complexity has been identified in composite bombs, where rhyolitic obsidian clasts contain regions of homogeneous hypocristalline glass in contact with complex microtextures that provide evidence of a clastic origin [Schipper et al. 2021; Wadsworth et al. 2022]. This clastogenic origin has been attributed to in-conduit multi-phased viscous sintering of the fine ash generated in the sub-surface throughout the eruption, likely due to reheating associated with the approach of the lava-forming melt [Schipper et al. 2021]. Degassing in sintered banded obsidians induced microlite crystallization in concentrated bands in opposite to less degassed microlite-free bands [Paisley et al. 2019], as we observe. Even though recent works find such features in 2011 Cordón Caulle products [Paisley et al. 2019; Schipper et al. 2021], in the present study

we identify the same textural characteristics in glass shards, including obsidians, from MH tephra.

Although in previous studies these obsidian particles were related to lithics reflecting the phreatomagmatic phases in MH tephra [Naranjo et al. 2017], the recycling processes of coeval (or almost coeval) particles during one eruption should not be dismissed, giving possibly to these MH glassy particles a juvenile character (see Section 4.2). This can result in significant participation of magma during the phreatomagmatic fragmentation processes with minor lithic abundance. The similar composition of the glass groundmass of these particles, both between light brown glass and obsidian, and between color bands of such particles, sustain the hypothesis of the juvenile character of these particles. Supporting this, the analyzed particles correspond to both the Puyehue stratovolcano (MH tephras) and the Cordón Caulle fissure system (CC tephras), both with too complex stratigraphies to allow the lithics to have such a homogenous composition. On the other hand, regardless of the character of the particles, the stratigraphy shows different types of eruption for MH (subplinian-phreatomagmatic) and CC (subplinian) deposits [Singer et al. 2008; Schipper et al. 2013; Naranjo et al. 2017], meaning that the fragmentation process involved in each tephra (MH vs. CC) formation would be different, giving rise to similar morphologies (see Section 4.2).

*Crystaloclasts.* They are represented by crystals and crystal fragments that have crystallized from magma, and at the time of fragmentation have been encapsulated by glass, showing thus vesicular textures on their surface [Heiken and Wohletz 1986]. Although the study of the mineral phases is not the focus of our work, they are present in all tephra levels, so future studies of the textures and mineral chemistry, both from crystaloclasts and phenocrysts, could provide insights into the eruptive triggers and magmatic processes (i.e. thermometry, thermobarometry, crystal textures) that originated each eruptive pulse of the PCCVC.

#### 4.1.2 *Lithic (cognate and recycled) particles*

*Brown pumice.* Even though brown pumice fragments have high degrees of vesicularity, similar to white saccharaoid pumice in some cases, *BP1* and *BP2* textures and the heterogeneity in geochemical composition of the glassy matrix could be associated with non-juvenile particles. *BP1* particles show juvenile volcanic texture but the glassy matrix is variable between MH and CC (~56 and 69 wt.% $SiO_2$, respectively;Supplementary Material 1 Table S4). Furthermore, this *BP1* type was identified as a scarce component in the deposits of the present work and further discussion about their origin requires more *BP* particle identification to discern if this textural type could be considered more abundant. This should be interesting since the assignation as juvenile components would imply other processes involved in their origin; i.e. magma mixing/mingling (in the case of MH tephra), not identified in this study nor previous [i.e. Schipper et al. 2021]. Type *BP2*, on the other hand, showed a broad chemical composition between particles (~59–72 wt.% $SiO_2$;Supplementary Material 1 Table S4) but with glass homogeneity within a single particle when it was possible to measure (i.e. between two and six measurements in some particles;Supplementary Material 1 Table S4). In addition, the complexity of textures resembles secondary processes, even though preserving their original volcanic rock textures. Extensive recrystallization, little remaining glassy matrix, presence of oxides on vesicle walls or along cracks truncating crystals and sectors of the matrix, elongation/collapse of vesicles, and patches of glass limited by microlites (Figure 7J–7L) are microtextures that can be interpreted as characteristic of heating-induced crystallization processes. These processes are related to the recycling of pyroclasts mainly in basalts to basaltic andesites [Deardorff and Cashman 2017], but are also observed here in more evolved compositions. Reheating processes activate thermal diffusion, allowing quite rapid recrystallization of plagioclases, pyroxenes, and oxides in the glassy matrix [Burkhard 2001; D'Oriano et al. 2013; 2014; Ruth et al. 2016; Deardorff and Cashman 2017]. This evidence suggests that dark brown pumice could be previously crystallized cognate fragments deposited in the proximity of the vent, affected by subsequent thermal reactivations, and incorporated at the time of the eruption as recycling of pyroclasts, both in MH and CC tephras. In addition, the geochemical patterns of lower overall enrichment in the *BP* multi-element diagram (Figure 12; *BP*(1960CC): this bulk geochemical data does not discriminate between *BP1* and *BP22*) and glass groundmass composition variation in individual fragments (Supplementary Material 1 Table S4), support the possibility of the cognate origin for *BP1* and *BP2* particles. According to the stratigraphy of the complex they could belong to older and less $SiO_2$ evolved units [Singer et al. 2008, and references therein]. A particular distinction among *BP2* particles is exemplified by those exhibiting patchy textures (Figure 7J–7L) and a rhyolitic glassy groundmass, resembling those sintering products from coeval juvenile particles identified in bombs ejected during the 2011 Cordón Caulle eruption [Schipper et al. 2021]. The lithic brown pumices particle type may include samples with juvenile characteristics corresponding to fragments emitted relatively recently [Benet et al. 2021]. Consequently, discerning the heterogeneity of components appears to be a challenging task.

*Scoria.* Besides the volcanic origin, textural and geochemical differences identified in scoria fragments within the same tephra level support their non-juvenile origin. Several works dealing with these deposits assign undoubtedly the lithic character to such scoriaceous particles as lava fragments with visible alteration and abundant crystals, both in MH and 2011CC deposits [Pistolesi et al. 2015; Naranjo et al. 2017]. According to the analysis of the bulk geochemistry, some scoria particles identified here may correspond to older units of the complex and therefore have a cognate origin. Moreover, *Sa2* particles have variable textures. Some porphyritic fragments with phenocrysts and microlite-free glassy groundmass <59 wt.% $SiO_2$ (Supplementary Material 1 Table S4) can represent lava fragments, as reported by Pistolesi et al. [2015] for altered clasts of scoriaceous texture for the 2011 Cordón Caulle deposit. Some microporphyritic clasts preserve the volcanic textures while others show evidence of recrystallization, with similar textures to those obtained by pyroclastic reheating experiments

[Burkhard 2001; D'Oriano et al. 2013; 2014; Ruth et al. 2016; Deardorff and Cashman 2017] and, like brown pumice, could represent recycled particles from recent eruptions. As we previously mentioned, no textural evidence of different magma mingling or chemical assimilation has been found to support the existence of magma mixing explaining this variability in particle association. In this sense, the different multi elemental patterns for scoria samples [Figure 12, *Sa*(MH8)], like for brown pumice, can represent the measurement of a mixture of morphologically similar particles with a variable compositional chemical range. For the aphyric *Sa1* particles, on the other hand, with a well-preserved rhyolitic glassy matrix (68–71 wt.% $SiO_2$), a juvenile origin cannot be ruled out. Similar rhyolitic particles of black color found in the 2011 Cordón Caulle deposit were explained by the oxidation state of the iron in the glass [Castro et al. 2013].

### 4.2 Puyehue stratovolcano vs. Cordón Caulle fissural system deposits

The MH unit has been assigned to the latest explosive eruption of the Puyehue composite cone, with a succession of powerful explosive subplinian to phreatomagmatic events that formed the modern crater [Singer et al. 2008; Naranjo et al. 2017]. At the location under study, the alternating is represented by fine to coarse dark obsidian-rich ash layers and lapilli pumice-rich light-colored layers. The changes in the abundance of the different types of components of each subunit provide information about the complex temporal interactions in the magma fragmentation processes that generated this multi-stratified deposit. Levels almost dominated by highly vesicular pumice particles with minor proportions of the dark components, like obsidians and lithics, represent the subplinian eruptive phases. Subplinian eruptions generally consist of pulses due to decoupling between magma supply and magma rate discharge generating mid-intensity discontinuous eruptions related to the release of batches of magma [Cioni et al. 2015; Todde et al. 2024]. This pulsatory nature of subplinian eruptions can generate the coexistence of variable vesicular fragments in deposits due to gradients in the degassing of magma in the conduit [Schipper et al. 2013; Pistolesi et al. 2015].

The fluctuations in the magma discharge may be an advantage for – or can be also affected due to – water entering the system, possibly as a consequence of the melting of the upper ice cap, as proposed by Naranjo et al. [2017] for previous Puyehue cone, favoring the phreatomagmatic pulses. Deformational load structures and armored lapilli at middle-distal facies evidence the phreatomagmatic character of the deposit [Naranjo et al. 2017; Alloway et al. 2022]. Even though the significant amount of fine ash (45–62 %) in dark layers of MH tephra is not a definitive diagnostic tool on its own, it is one of the several features of phreatomagmatic deposits [White and Valentine 2016]. The high abundance of blocky (obsidians) to low vesicular (brown glass) shaped particles in these layers can be related to fragmentation after the decompression wave produced by molten-coolant (magma-water) interaction with a brittle-type fragmentation mechanism in rhyolite magmas, due to high viscosities [Zimanowski et al. 2015]. In this sense, Naranjo et al. [2017] associate the large volume of fine ash in MH with fragmentation induced by simultaneous phreatomagmatic explosions or pulses at different parts of the collapsing crater. Moreover, the high vesicularity of the magma batches evidenced by the highly vesicular pumice, may have facilitated the brittle fragmentation during magma-water interactions. Relatively low deformation energy is required to fracture solid, highly vesicular material, resulting in the emission of fine, dense ash fragments inherited from the initial vesicular magma [Zimanowski et al. 2015; Thivet et al. 2022]. Sharp changes in grain size between MH subunits favor abrupt shifts in both eruption intensity and magma:water ratio [Houghton et al. 2010]. Further studies on the glassy fine ash should demonstrate the presence of active particles as direct evidence of phreatomagmatic fragmentation [Zimanowski et al. 2015].

In MH, the dark-fine deposits were defined as lithic-rich layers [Singer et al. 2008; Naranjo et al. 2017]. In this work, on the other hand, obsidian and brown glassy particles of homogeneous composition resemble typical juvenile fragments which, together with a significant amount of glass-covered crystals, should result from the fragmentation of a degassed-porphyritic magma in contact with water. Also, the complex textures (banding, patchy textures) identified in the glass population were recently associated with the sintering of fine ash (juvenile) inside the conduit, in bombs from the 2011 Cordón Caulle eruption [Paisley et al. 2019; Schipper et al. 2021] related to effusive/explosive eruptive transitions [Wadsworth et al. 2022]; this sintering process could be facilitated through the generation of fine ash related to fragmentation mechanisms. In comparison with such studies, our observations provide information about the possible juvenile character of glassy brown and obsidian particles from MH, rather than being considered as lithics. However, the analyses of the componentry along MH subunits evidence that *GS* and *Ob* are the dominant particles during the first subunits which would be, in theory, more related to the opening and widening of the conduit. In this line of thought, possibly both processes have occurred, and "glassy lithics" with juvenile-like textural features originating from the destruction of a previous rhyolitic dome [Naranjo et al. 2017] can occur together with juvenile fragments from a coherent magma fragmenting during ascent. An analogy with the process of sintering and welding of fragmented materials sealing the shallow conduit [as proposed by Schipper et al. 2021; Wadsworth et al. 2022] could be inferred during periods of low magma supply. Adding the effect of water entering the conduit, the fragmentation of a coherent clastogenic magma could have been generated. As far as we know, our observations are the first textural descriptions of MH particles, suggesting an important challenge in the definition of this lithic vs. juvenile origin from the particles as an indicator of the degree of magma participation in the explosive events. In this sense, due to the remarkable glass homogeneous composition, a detailed subunit-by-subunit textural study of this kind of particles should be performed to discriminate between juvenile and those lithics from the vent opening previous units. Although detailed reconstructions of moderate to large-scale rhyolite eruptions are limited, several examples of phreatomagmatic/magmatic can be identified in

the literature evidencing the complexity of the processed involved [Houghton et al. 2010; Dellino et al. 2012].

At the study site, 2011CC is coarser than the 1960CC tephra deposit, and 2011CC mode is composed almost totally of pumice. However, if in 2011CC the grain size fraction similar to the 1960CC mode is analyzed, the same componentry is observed, with the presence mainly of pumice, scoria, crystals, and obsidians. The observed differences just respond to the variable intensity of both eruptions [González-Ferrán 1995; Naranjo et al. 2017] and probably some difference in the direction of dispersion [Petit-Breuilh Sepúlveda 2004]. Even considering that both events correspond to different exit vents, the componentry is comparable as both break through the same stratigraphy from a unique magma reservoir, and fragmentation processes are characterized as dry or magmatic dominant. Few observations on small-moderate rhyolitic eruptions suggest that the heterogeneity observed in components is a common feature, along with a complex tephra deposits stratigraphy, due to variable intensity of explosive activity, complex magma outgassing history, hybrid eruptions, unsteady column dynamics, long duration of events, variable wind direction, among other factors [Schipper et al. 2013; Pistolesi et al. 2015, and references therein]. The same component heterogeneity was identified in lake sequences at distal positions for the latest Cordón Caulle eruptions [1960, 1921–22, mid-18$^{th}$ century deposit; Daga et al. 2010; 2012; Sosa et al. 2024]. The 2011CC eruption was widely studied, discussing the existence of a large range of vesicular degrees in juvenile clasts associated with the existence of sub-vents, shifts in eruption intensity, and the occurrence of explosive-effusive processes [Schipper et al. 2013; Wadsworth et al. 2022]. In these vents, magma could ascend at different speeds. Those of slow ascent allowed the degasification of the magma with greater efficiency, resulting in the absence of vesicles while faster ascending zones generated high vesicular degree producing pumice clasts [Schipper et al. 2013; Pistolesi et al. 2015]. However, multi-generational fragmentation and sintering were recently proposed as characteristic processes within the shallow conduit during the explosive-effusive transition for the 2011 Cordón Caulle event; this process associates the presence of lava with rates of melt fracture and sintering rather than outgassing through permeable bubble networks in melt body [Schipper et al. 2021]. In that way, Crozier et al. [2022] reinforce the role of degassing through magmatic fractures accompanying localized fragmentation and welding (or sintering) under conditions that enable effusive behavior. Anyway, these complex processes could explain the variety of recrystallization textures and the presence of cognate and lithic fragments found within each level.

In comparison, deposits corresponding to the Cordón Caulle fissural system, representing the most recent activity of the PCCVC, showed component similarity, particularly with the subplinian eruptive phases from the last Puyehue eruption, with no supposed influence of water in the Cordón Caulle system. The geochemical pattern is the same for juvenile components from both the stratovolcano and the fissural system. It is common in calc-alkaline magmas of shallow arcs, and the anomalies are controlled by the crystallization of specific mineral phases. Negative anomalies in Eu and Sr indicate low oxygen activities and plagioclase crystallization in the magmatic chamber [$Ca^{2+}$ compatible behavior; Rollinson 1993]. Ti and Ta negative anomalies may indicate crystallization of ilmenite and cortical contamination, respectively [Wilson 1989]. All these features are the fingerprint of the postglacial products from PCCVC (Figure 12). Together with the relative invariant latest geochemical fingerprint, it is suggested that the magmatic source has remained unchanged throughout the last millennium [Gerlach et al. 1988; Jicha et al. 2007; Singer et al. 2008]. Also, considering that the most recent rhyodacite and rhyolite lavas and pyroclasts were restricted to the Cordón Caulle fissure, and such products are compositionally and isotopically similar to post-glacial lavas from Puyehue volcano (without recent activity), a shifting of the volcanism to the northwest was suggested [Gerlach et al. 1988]. Although CC and MH erupted from different exit conduits and despite the range of silica contents (throughout their evolution), both define similar geochemical trends that can be related to fractional crystallization processes from a common parental source since 100 ky, and the eruptive style seems to be independent of the geochemical signatures in the PCCVC [Lara and Moreno 2006].

### 4.3 Tephrochronological implications

A wide variety of particle types, textures, and vesicular degrees were identified within each tephra level. Typical juvenile morphologies of magmatic and phreatomagmatic explosive processes have been recognized in all types of particles analyzed, and in all tephra deposits, coexisting with particles with juvenile-like morphologies but non-juvenile microtextures. White and pale-beige pumice fragments and glass shards are the typical juvenile components in these deposits, while brown pumice and scoria represent mainly (although not strictly) non-juvenile particles due to identified recrystallization and flow textures (like recycled or sintered particles or lava fragments). Their proportions vary according to the dominant mechanism of formation of units/subunits.

This aspect can also be significant when proposing volcanic sources to correlate with sedimentary units in distant areas. Geochemical fingerprinting of glassy shards is the most commonly used link between tephras to their source volcano, due to the regional/continental dispersion they can reach [Lowe et al. 2017]. However, in proximal to medial zones, the componentry of tephra deposits can facilitate the correlations, particularly in areas close to volcanic zones with high eruptive frequency and/or the existence of several deposits from the same volcanoes. This occurs in the study region, where the historical/prehistorical eruptions from Cordón Caulle fissure, for example, show a wide regional dispersion and limited range in geochemical composition [Gerlach et al. 1988; Castro et al. 2013; Sosa et al. 2024, among others]. The discrimination between the most recent deposits, in most cases, can be difficult when the successive record of eruptions is incomplete.

The most recent tephra deposits from Cordón Caulle (1921, 1960, and an event in the mid-18$^{th}$ century) were identified in several lacustrine sequences at mid to distal PCCVC locations both to the east and west, exhibiting similar morphological and geochemical variability in their components mainly

in the eastward downwind records [Bertrand et al. 2008; Daga et al. 2010; 2012; 2014; Sosa et al. 2024]. In such works, although the different types of particles were mainly considered as juveniles, their identification resulted in a valuable tool for correlation purpose and chronostratigraphic application. Here lies the importance of characterizing the components in both proximal and medial deposits, as well as distal ones. Recently, a deposit correlating with an 18$^{th}$ century Cordón Caulle eruption (an event mentioned in historical records) was identified in lacustrine records, with no evidence found in outcrops [Sosa et al. 2024]. Lake sequences, even at remote positions, can provide complete and higher resolution eruptive archives than outcrop stratigraphy, being also generally responsive to radiocarbon dating [Bertrand et al. 2014; Alloway et al. 2022]; however, their interpretations are greatly favored if the proximal pyroclastic deposits are appropriately characterized.

## 5 Conclusions

The latest eruption of the Cordón Caulle fissure system in 2011 gave the possibility of great advances in studies about the deposit and the involved eruptive processes while, as far as we know, our observations are the first textural analyses performed in the tephra deposit related to the formation of the current crater of Puyehue volcano. Even though their different emission centers and eruptive styles, great similarity was found between their pyroclastic products. On the other hand, the variability of features within each tephra layer, such as the type of particles and their vesicular arrangements, linked to specific magma fragmentation conditions, evidence the complexity of the extrusion processes in the PCCVC over the last millennium. The particles analyzed in this work are associated with explosive processes, via both dry and wet mechanisms.

The study of the external morphology of particles is an important but limited tool for identifying their origin and source volcano. However, the mechanisms that generate these particles can preserve characteristic features in pyroclasts, fundamental for understanding volcanic processes and determining the eruptive style. Textural studies, therefore, combined with groundmass glass composition, have shown potential in differentiating juvenile from non-juvenile particles. Specifically, vesicular brown glass shards are generally associated with a juvenile origin in pyroclastic deposits. Nevertheless, the variations in the internal textures observed in these particles are typically indicative of a non-juvenile origin, such as recycled pyroclasts, broken lavas or obsidian fragments. However, comparison with recent studies on products from the 2011 Cordón Caulle eruption allows us to infer that glass shards can be possibly generated from recycling processes, or sintering, of coeval (or almost coeval) particles during a single eruption, highlighting their juvenile character.

Since the dominant fragmentation mechanism differs for the Cordón Caulle system and Puyehue volcano from dry to wet, respectively, the similarity of the particles is striking. At least, the possibility that part of the components previously defined as lithics for MH tephra may correspond to juvenile material must be considered. Moreover, the presence of such textures throughout the sedimentary column suggests that contemporary pyroclastic reheating and sintering processes could be a recurrent phenomenon in the various tephra emission centers. This is fundamental to avoid incorrect interpretations of the amount of juvenile material emitted in an eruption. These results enhance our understanding of the deposits and prompt reconsiderations of previous assumptions. Nevertheless, the variability of tephra deposits components, whether juvenile or lithic, is a highly valuable tool for tephra-correlation purposes, potentially characteristic of the PCCVC.

From a volcanological perspective, the high abundance of highly vesicular pumice throughout the sedimentary column suggests that decompression-driven gas exsolution was the main process in all postglacial eruptive events of the PCCVC, mainly at the Cordón Caulle system, as reflected in the type of eruptions. Additionally, wet fragmentation mechanisms producing low-vesicular to blocky fragments due to influence of water have alternated with magmatic mechanisms, particularly in the last event from Puyehue volcano. However, changes in effusive and explosive eruptive styles within a single eruption should be considered as a hypothesis if a diversity of textures are found, such as those presented in this study. A detailed textural and geochemical study of the abundance and variation of different components between subunits could enhance our understanding of the multi-phased events that shaped the current configuration of the Puyehue stratocone and the potential reasons of the shift of volcanism to the Cordón Caulle fissure system.

## Author Contributions

WA and RD made contributions to the conceptualization, participated in the fieldwork and subsequent sample analyses, which encompassed grain size determinations, SEM and INAA sample conditioning, and interpretation of geochemical and image data. WA spearheaded the manuscript preparation, with the support of RD. AD supported the sample preparation and contributed to the development of the idea, data interpretation, and manuscript editing. SRG and GG conducted the INAA measurements and participated in the manuscript writing.

## Acknowledgements

The authors wish to express their gratitude to Eber Cristofolini and Matías Barzola from the Departamento de Geología, Universidad Nacional de Río Cuarto, for their collaboration in sample preparation; to the Departamento Caracterización de Materiales, Centro Atómico Bariloche, for the support in SEM studies; and to the reactor RA-6 staff for their assistance in sample analysis. We would like to express our sincere gratitude to Jamie Farquharson, Samantha Tramontano, and an anonymous reviewer for their insightful comments and constructive suggestions, which significantly enhanced both the structure and clarity of this manuscript. We are grateful to Nahuel Huapi National Park Administration for allowing fieldwork (Permission 1490). This work was partially funded by PICT 2016-0298 and PICT 2019-03000 projects.

## Data Availability

All data is available in the images, tables, and Supplementary Material provided in the online version of the article.

## References

Alloway, B. V., N. J. G. Pearce, P. I. Moreno, G. Villarosa, I. A. Jara, C. A. Henríquez, E. A. Sagredo, M. T. Ryan, and V. Outes (2022). "Refinement of the tephrostratigraphy straddling the northern Patagonian Andes (40–41°S): new tephra markers, reconciling different archives and ascertaining the timing of piedmont deglaciation". *Journal of Quaternary Science* 37(3), pages 441–477. DOI: 10.1002/jqs.3389.

Amigo, Á., L. E. Lara, and V. C. Smith (2013). "Holocene record of large explosive eruptions from Chaitén and Michinmahuida Volcanoes, Chile". *Andean Geology* 40(2), pages 227–248. DOI: 10.5027/andgeoV40n2-a03.

Benet, D., F. Costa, G. Pedreros, and C. Cardona (2021). "The volcanic ash record of shallow magma intrusion and dome emplacement at Nevados de Chillán Volcanic complex, Chile". *Journal of Volcanology and Geothermal Research* 417, article 107308. DOI: 10.1016/j.jvolgeores.2021.107308.

Bertrand, S., J. Castiaux, and E. Juvigné (2008). "Tephrostratigraphy of the late glacial and Holocene sediments of Puyehue Lake (southern volcanic zone, Chile, 40 °S)". *Quaternary Research* 70(3), pages 343–357. DOI: 10.1016/j.yqres.2008.06.001.

Bertrand, S., R. Daga, R. Bedert, and K. Fontijn (2014). "Deposition of the 2011–2012 Cordón Caulle tephra (Chile, 40°S) in lake sediments: Implications for tephrochronology and volcanology". *Journal of Geophysical Research: Earth Surface* 119(12), pages 2555–2573. DOI: 10.1002/2014JF003321.

Burkhard, D. J. M. (2001). "Crystallization and oxidation of Kilauea basalt glass: Processes during reheating experiments". *Journal of Petrology* 42(3), pages 507–527. DOI: 10.1093/petrology/42.3.507.

Castro, J. M., C. I. Schipper, S. P. Mueller, A. S. Militzer, A. Amigo, C. S. Parejas, and D. Jacob (2013). "Storage and eruption of near-liquidus rhyolite magma at Cordón Caulle, Chile". *Bulletin of Volcanology* 75, article 702. DOI: 10.1007/s00445-013-0702-9.

Cioni, R., M. Pistolesi, and M. Rosi (2015). "Plinian and subplinian eruptions". *The Encyclopedia of Volcanoes*. Elsevier, pages 519–535. DOI: 10.1016/B978-0-12-385938-9.00029-8.

Crozier, J., S. Tramontano, P. Forte, S. J. C. Oliva, H. M. Gonnermann, E. Lev, M. Manga, M. Myers, E. Rader, P. Ruprecht, et al. (2022). "Outgassing through magmatic fractures enables effusive eruption of silicic magma". *Journal of Volcanology and Geothermal Research* 430, article 107617. DOI: 10.1016/j.jvolgeores.2022.107617.

D'Oriano, C., A. Bertagnini, R. Cioni, and M. Pompilio (2014). "Identifying recycled ash in basaltic eruptions". *Scientific Reports* 4, article 5851. DOI: 10.1038/srep05851.

D'Oriano, C., M. Pompilio, A. Bertagnini, R. Cioni, and M. Pichavant (2013). "Effects of experimental reheating of natural basaltic ash at different temperatures and redox conditions". *Contributions to Mineralogy and Petrology* 165(5), pages 863–883. DOI: 10.1007/s00410-012-0839-0.

Daga, R., S. Ribeiro Guevara, M. Sánchez, and M. Arribére (2006). "Geochemical characterization of volcanic ashes from recent events in Northern Patagonia Andean Range by INAA". *Journal of Radioanalytical and Nuclear Chemistry* 270(3), pages 677–694. DOI: 10.1007/s10967-006-0447-4.

Daga, R., A. Castro, J. De La Rosa, S. Ribeiro Guevara, M. L. Sanchez, and M. Arribere (2012). "Heterogeneidades texturales y composicionales en productos piroclásticos de la erupción de 1960 del sistema Cordón Caulle (40° 30'S, 72° 10'O)". *Revista de la Asociación Geológica Argentina* 69(4), pages 496–507.

Daga, R., S. R. Guevara, M. L. Sánchez, and M. Arribére (2010). "Tephrochronology of recent events in the Andean Range (northern Patagonia): spatial distribution and provenance of lacustrine ash layers in the Nahuel Huapi National Park". *Journal of Quaternary Science* 25(7), pages 1113–1123. DOI: 10.1002/jqs.1378.

Daga, R., S. Ribeiro Guevara, D. G. Poire, and M. Arribére (2014). "Characterization of tephras dispersed by the recent eruptions of volcanoes Calbuco (1961), Chaitén (2008) and Cordón Caulle Complex (1960 and 2011), in Northern Patagonia". *Journal of South American Earth Sciences* 49, pages 1–14. DOI: 10.1016/j.jsames.2013.10.006.

Deardorff, N. and K. Cashman (2017). "Rapid crystallization during recycling of basaltic andesite tephra: timescales determined by reheating experiments". *Scientific Reports* 7, article 46364. DOI: 10.1038/srep46364.

Del Carlo, P., A. Di Roberto, M. D'Orazio, M. Petrelli, A. Angioletti, G. Zanchetta, V. Maggi, R. Daga, M. Nazzari, and S. Rocchi (2018). "Late Glacial-Holocene tephra from southern Patagonia and Tierra del Fuego (Argentina, Chile): A complete textural and geochemical fingerprinting for distal correlations in the Southern Hemisphere". *Quaternary Science Reviews* 195, pages 153–170. DOI: 10.1016/j.quascirev.2018.07.028.

Dellino, P., M. Gudmundsson, G. Larsen, D. Mele, J. Stevenson, T. Thordarson, and B. Zimanowski (2012). "Ash from the Eyjafjallajökull eruption (Iceland): Fragmentation processes and aerodynamic behavior". *Journal of Geophysical Research: Solid Earth* 117(B9), article B00C04. DOI: 10.1029/2011JB008726.

Di Roberto, A., B. Scateni, G. Di Vincenzo, M. Petrelli, G. Fisauli, S. J. Barker, P. Del Carlo, F. Colleoni, D. K. Kulhanek, R. McKay, L. De Santis, and The IODP Expedition 374 Scientific Party (2021). "Tephrochronology and provenance of an early Pleistocene (calabrian) tephra from IODP Expedition 374 Site U1524, Ross Sea (Antarctica)". *Geochemistry, Geophysics, Geosystems* 22(8), article e2021GC009739. DOI: 10.1029/2021GC009739.

Fisher, R. V. (1961). "Proposed classification of volcaniclastic sediments and rocks". *Geological Society of America Bulletin* 72(9), pages 1409–1414. DOI: 10.1130/0016-7606(1961)72[1409:PCOVSA]2.0.CO;2.

Fontijn, K., S. M. Lachowycz, H. Rawson, D. M. Pyle, T. A. Mather, J. A. Naranjo, and H. Moreno-Roa (2014). "Late Quaternary tephrostratigraphy of southern Chile and Argentina". *Quaternary Science Reviews* 89, pages 70–84. DOI: 10.1016/j.quascirev.2014.02.007.

Fontijn, K., H. Rawson, M. Van Daele, J. Moernaut, A. M. Abarzúa, K. Heirman, S. Bertrand, D. M. Pyle, T. A. Mather, M. De Batist, J.-A. Naranjo, and H. Moreno (2016). "Synchronisation of sedimentary records using tephra: A postglacial tephrochronological model for the Chilean Lake District". *Quaternary Science Reviews* 137, pages 234–254. DOI: 10.1016/j.quascirev.2016.02.015.

Gerlach, D. C., F. A. Frey, H. Moreno-Roa, and L. Lopez-Escobar (1988). "Recent volcanism in the Puyehue–Cordon Caulle region, Southern Andes, Chile (40.5°S): Petrogenesis of evolved lavas". *Journal of Petrology* 29(2), pages 333–382. DOI: 10.1093/petrology/29.2.333.

González, P. D. (2008). "Geología de los cuerpos ígneos". Serie B Didáctica y Complementaria N° 29. Asociación Geológica Argentina. Chapter Texturas de los cuerpos ígneos, pages 167–195.

González-Ferrán, O. (1995). "Volcanes de Chile. Instituto Geográfico Militar". *Santiago* 635.

Heiken, G. and K. Wohletz (1986). *Volcanic Ash*. University of California Press, Berkley.

Houghton, B. F., R. J. Carey, K. V. Cashman, C. J. Wilson, B. J. Hobden, and J. E. Hammer (2010). "Diverse patterns of ascent, degassing, and eruption of rhyolite magma during the 1.8 ka Taupo eruption, New Zealand: Evidence from clast vesicularity". *Journal of Volcanology and Geothermal Research* 195(1), pages 31–47. DOI: 10.1016/j.jvolgeores.2010.06.002.

Hu, R., F. Li, H. Yu, and J. Yang (2019). "Application of ImageJ in the rock thin section image analysis: the separation and quantitative calculation of crystal-glass two phases". *Journal of Earth Sciences Environmental Studies* 4 (3), pages 609–616. DOI: 10.25177/JESES.4.3.RA.502.

Iverson, N. A., D. Kalteyer, N. W. Dunbar, A. Kurbatov, and M. Yates (2017). "Advancements and best practices for analysis and correlation of tephra and cryptotephra in ice". *Quaternary Geochronology* 40, pages 45–55. DOI: 10.1016/j.quageo.2016.09.008.

Jicha, B. R., B. S. Singer, B. L. Beard, C. M. Johnson, H. Moreno-Roa, and J. A. Naranjo (2007). "Rapid magma ascent and generation of $^{230}$Th excesses in the lower crust at Puyehue–Cordón Caulle, Southern Volcanic Zone, Chile". *Earth and Planetary Science Letters* 255(1-2), pages 229–242. DOI: 10.1016/j.epsl.2006.12.017.

Jones, T. J. and J. K. Russell (2017). "Ash production by attrition in volcanic conduits and plumes". *Scientific Reports* 7(1), article 5538. DOI: 10.1038/s41598-017-05450-6.

Kratzmann, D. J., S. Carey, R. Scasso, and J.-A. Naranjo (2009). "Compositional variations and magma mixing in the 1991 eruptions of Hudson volcano, Chile". *Bulletin of Volcanology* 71(4), pages 419–439. DOI: 10.1007/s00445-008-0234-x.

Lara, L. E., J. A. Naranjo, and H. Moreno (2004). "Rhyodacitic fissure eruption in Southern Andes (Cordón Caulle; 40.5°S) after the 1960 (Mw:9.5) Chilean earthquake: a structural interpretation". *Journal of Volcanology and Geothermal Research* 138(1-2), pages 127–138. DOI: 10.1016/j.jvolgeores.2004.06.009.

Lara, L. E. and H. Moreno (2006). *Geología del Complejo Volcánico Puyehue-Cordón Caulle, Región de los Lagos*. Servicio Nacional de Geología y Minería, Carta Geológica de Chile, Serie Geología Básica.

Lautze, N. C. and B. F. Houghton (2007). "Linking variable explosion style and magma textures during 2002 at Stromboli volcano, Italy". *Bulletin of Volcanology* 69(4), pages 445–460. DOI: 10.1007/s00445-006-0086-1.

Lowe, D. J. (2011). "Tephrochronology and its application: A review". *Quaternary Geochronology* 6(2), pages 107–153. DOI: 10.1016/j.quageo.2010.08.003.

Lowe, D. J., N. J. G. Pearce, M. A. Jorgensen, S. C. Kuehn, C. A. Tryon, and C. L. Hayward (2017). "Correlating tephras and cryptotephras using glass compositional analyses and numerical and statistical methods: Review and evaluation". *Quaternary Science Reviews* 175, pages 1–44. DOI: 10.1016/j.quascirev.2017.08.003.

Manzotti, P., D. Regis, D. C. Petts, R. Graziani, and M. Polivchuk (2024). "Formation of multistage garnet grains by fragmentation and overgrowth constrained by microchemical and microstructural mapping". *Journal of Metamorphic Geology* 42(4), pages 471–496. DOI: 10.1111/jmg.12761.

Matsumoto, K. and N. Geshi (2021). "Shallow crystallization of eruptive magma inferred from volcanic ash microtextures: A case study of the 2018 eruption of Shinmoedake volcano, Japan". *Bulletin of Volcanology* 83, article 31. DOI: 10.1007/s00445-021-01451-6.

McDonough, W. F. and S.-S. Sun (1995). "The composition of the Earth". *Chemical Geology* 120(3-4), pages 223–253. DOI: 10.1016/0009-2541(94)00140-4.

McPhie, J. (1993). *Volcanic textures: a guide to the interpretation of textures in volcanic rocks*.

Moreno Roa, H. (1977). "Geología del área volcánica Puyehue Carrán en Los Andes del sur de Chile". PhD thesis. Universidad De Chile, Santiago.

Moriizumi, M., S. Nakashima, S. Okumura, and Y. Yamanoi (2009). "Color-change processes of a plinian pumice and experimental constraints of color-change kinetics in air of an obsidian". *Bulletin of Volcanology* 71, pages 1–13. DOI: 10.1007/s00445-008-0202-5.

Mujin, M. and M. Nakamura (2014). "A nanolite record of eruption style transition". *Geology* 42(7), pages 611–614. DOI: 10.1130/G35553.1.

Naranjo, J. A., B. S. Singer, B. R. Jicha, H. Moreno, and L. E. Lara (2017). "Holocene tephra succession of Puyehue-Cordón Caulle and Antillanca/Casablanca volcanic complexes, southern Andes (40–41°S)". *Journal of Volcanology and Geothermal Research* 332, pages 109–128. DOI: 10.1016/j.jvolgeores.2016.11.017.

Naranjo, J. A. and C. R. Stern (1998). "Holocene explosive activity of Hudson Volcano, southern Andes". *Bulletin of Volcanology* 59(4), pages 291–306. DOI: 10.1007/s004450050193.

– (2004). "Holocene tephrochronology of the southernmost part (42°30'–45°S) of the Andean Southern Volcanic Zone". *Revista geológica de Chile* 31(2). DOI: 10.4067/S0716-02082004000200003.

Paisley, R., K. Berlo, J. Whattam, C. I. Schipper, and H. Tuffen (2019). "Degassing-induced chemical heterogeneity at the 2011–2012 Cordón Caulle eruption". *Volcanica* 2(2), pages 211–237. DOI: 10.30909/vol.02.02.211237.

Paredes-Mariño, J., K. J. Dobson, G. Ortenzi, U. Kueppers, D. Morgavi, M. Petrelli, K.-U. Hess, K. Laeger, M. Porreca, A. Pimentel, and D. Perugini (2017). "Enhancement of eruption explosivity by heterogeneous bubble nucleation triggered by magma mingling". *Scientific Reports* 7, article 16897. DOI: 10.1038/s41598-017-17098-3.

Paruelo, J. M., A. Beltrán, E. Jobbágy, O. E. Sala, and R. A. Golluscio (1998). "The climate of Patagonia general patterns and controls on biotic processes". *Ecologia Austral* 8(2).

Petit-Breuilh Sepúlveda, M. E. (2004). *La Historia Eruptiva de los Volcanes Hispanoamericanos (Siglos XVI al XX): El Modelo Chileno*. Serie Casa de los Volcanes Nº. 8. Ed. Servicio de Publicaciones Exmo. Cabildo Insular de Lanzarote.

Pistolesi, M., R. Cioni, C. Bonadonna, M. Elissondo, V. Baumann, A. Bertagnini, L. Chiari, R. Gonzales, M. Rosi, and L. Francalanci (2015). "Complex dynamics of small-moderate volcanic events: the example of the 2011 rhyolitic Cordón Caulle eruption, Chile". *Bulletin of Volcanology* 77, article 3. DOI: 10.1007/s00445-014-0898-3.

Platz, T., S. J. Cronin, K. V. Cashman, R. B. Stewart, and I. E. M. Smith (2007). "Transition from effusive to explosive phases in andesite eruptions — A case-study from the AD1655 eruption of Mt. Taranaki, New Zealand". *Journal of Volcanology and Geothermal Research* 161(1-2), pages 15–34. DOI: 10.1016/j.jvolgeores.2006.11.005.

Polacci, M., L. Pioli, and M. Rosi (2003). "The Plinian phase of the Campanian Ignimbrite eruption (Phlegrean Fields, Italy): Evidence from density measurements and textural characterization of pumice". *Bulletin of Volcanology* 65, pages 418–432. DOI: 10.1007/s00445-002-0268-4.

Rawson, H., J. A. Naranjo, V. C. Smith, K. Fontijn, D. M. Pyle, T. A. Mather, and H. Moreno (2015). "The frequency and magnitude of post-glacial explosive eruptions at Volcán Mocho-Choshuenco, southern Chile". *Journal of Volcanology and Geothermal Research* 299, pages 103–129. DOI: 10.1016/j.jvolgeores.2015.04.003.

Rojas, F., J. Browning, H. Tuffen, J. Cembrano, J. Espinosa-Leal, H. E. Unwin, T. M. Mitchell, K. Hofer-Apostolidis, and P. G. Meredith (2024). "Textural evidence of fragmentation and densification processes in a fossilised shallow conduit on the flank of Nevados de Chillán Volcanic Complex". *Journal of Volcanology and Geothermal Research* 447, article 108028. DOI: 10.1016/j.jvolgeores.2024.108028.

Rollinson, H. R. (1993). *Using geochemical data: Evaluation, presentation, interpretation*. Routledge. DOI: 10.4324/9781315845548.

Rotella, M. D., C. J. N. Wilson, S. J. Barker, K. V. Cashman, B. F. Houghton, and I. C. Wright (2014). "Bubble development in explosive silicic eruptions: Insights from pyroclast vesicularity textures from Raoul volcano (Kermadec arc)". *Bulletin of Volcanology* 76, article 826. DOI: 10.1007/s00445-014-0826-6.

Rust, A. C. and K. V. Cashman (2007). "Multiple origins of obsidian pyroclasts and implications for changes in the dynamics of the 1300 B.P. eruption of Newberry Volcano, USA". *Bulletin of Volcanology* 69(8), pages 825–845. DOI: 10.1007/s00445-006-0111-4.

Ruth, D. C., E. Cottrell, J. A. Cortes, K. A. Kelley, and E. S. Calder (2016). "From passive degassing to violent Strombolian eruption: the case of the 2008 eruption of Llaima volcano, Chile". *Journal of Petrology* 57(9), pages 1833–1864. DOI: 10.1093/petrology/egw063.

Schindelin, J., I. Arganda-Carreras, E. Frise, V. Kaynig, M. Longair, T. Pietzsch, S. Preibisch, C. Rueden, S. Saalfeld, B. Schmid, J.-Y. Tinevez, D. J. White, V. Hartenstein, K. Eliceiri, P. Tomancak, and A. Cardona (2012). "Fiji: an open-source platform for biological-image analysis". *Nature Methods* 9, pages 676–682. DOI: 10.1038/nmeth.2019.

Schipper, C. I., J. M. Castro, B. M. Kennedy, H. Tuffen, J. Whattam, F. B. Wadsworth, R. Paisley, R. H. Fitzgerald, E. Rhodes, L. N. Schaefer, P. A. Ashwell, P. Forte, G. Seropian, and B. V. Alloway (2021). "Silicic conduits as supersized tuffisites: Clastogenic influences on shifting eruption styles at Cordón Caulle volcano (Chile)". *Bulletin of Volcanology* 83, article 11. DOI: 10.1007/s00445-020-01432-1.

Schipper, C. I., J. M. Castro, H. Tuffen, M. R. James, and P. How (2013). "Shallow vent architecture during hybrid explosive–effusive activity at Cordón Caulle (Chile, 2011–12): Evidence from direct observations and pyroclast textures". *Journal of Volcanology and Geothermal Research* 262, pages 25–37. DOI: 10.1016/j.jvolgeores.2013.06.005.

Shea, T., B. F. Houghton, L. Gurioli, K. V. Cashman, J. E. Hammer, and B. J. Hobden (2010). "Textural studies of vesicles in volcanic rocks: An integrated methodology". *Journal of Volcanology and Geothermal Research* 190(3-4), pages 271–289. DOI: 10.1016/j.jvolgeores.2009.12.003.

Singer, B. S., B. R. Jicha, M. A. Harper, J. A. Naranjo, L. E. Lara, and H. Moreno-Roa (2008). "Eruptive history, geochronology, and magmatic evolution of the Puyehue-Cordón Caulle volcanic complex, Chile". *Geological Society of America Bulletin* 120(5-6), pages 599–618. DOI: 10.1130/B26276.1.

Sosa, D. S., R. Daga, A. Demichelis, W. Alfonzo, and S. R. Guevara (2024). "Extending the mid-18$^{th}$ century eruptive record of the Cordón Caulle Volcanic Complex (40, 5° S) through the study of three lake sedimentary sequences". *Journal of South American Earth Sciences* 137, article 104837. DOI: 10.1016/j.jsames.2024.104837.

Stern, C. R. (2004). "Active Andean volcanism: Its geologic and tectonic setting". *Revista geológica de Chile* 31(2). DOI: 10.4067/S0716-02082004000200001.

Stern, C. R. (2008). "Holocene tephrochronology record of large explosive eruptions in the southernmost Patagonian Andes". *Bulletin of Volcanology* 70, pages 435–454. DOI: 10.1007/s00445-007-0148-z.

Thivet, S., J. Carlier, L. Gurioli, A. Di Muro, P. Besson, M. Smietana, G. Boudon, P. Bachèlery, J. Eychenne, and J.-M. Nedelec (2022). "Magmatic and phreatomagmatic contributions on the ash-dominated basaltic eruptions: Insights from the April and November–December 2005 paroxysmal events at Karthala volcano, Comoros". *Journal of Volcanology and Geothermal Research* 424, article 107500. DOI: 10.1016/j.jvolgeores.2022.107500.

Todde, A., J. N. Procter, and G. Kereszturi (2024). "Reconstructing episodic and multi-vent, rhyolitic eruptions: The ~1314 CE Kaharoa eruption of the Tarawera Dome Complex, Okataina Caldera (New Zealand)". *Journal of Volcanology and Geothermal Research* 451, article 108107. DOI: 10.1016/j.jvolgeores.2024.108107.

Toramaru, A., S. Noguchi, S. Oyoshihara, and A. Tsune (2008). "MND (microlite number density) water exsolution rate meter". *Journal of Volcanology and Geothermal Research* 175(1-2), pages 156–167. DOI: 10.1016/j.jvolgeores.2008.03.035.

Visalli, R., M. Giuffrida, and M. Viccaro (2023). "Unraveling textural and chemical features in volcanic rocks through advanced image processing: A case study from the 2019 paroxysmal eruptions of stromboli". *Geochemistry, Geophysics, Geosystems* 24(3), article e2022GC010774. DOI: 10.1029/2022GC010774.

Wadsworth, F. B., E. W. Llewellin, J. M. Castro, H. Tuffen, C. I. Schipper, J. E. Gardner, J. Vasseur, A. Foster, D. E. Damby, I. M. McIntosh, et al. (2022). "A reappraisal of explosive–effusive silicic eruption dynamics: syn-eruptive assembly of lava from the products of cryptic fragmentation". *Journal of Volcanology and Geothermal Research* 432, article 107672. DOI: 10.1016/j.jvolgeores.2022.107672.

Watt, S. F. L., D. M. Pyle, J. A. Naranjo, G. Rosqvist, M. Mella, T. A. Mather, and H. Moreno (2011). "Holocene tephrochronology of the Hualaihue region (Andean southern volcanic zone, ~42° S), southern Chile". *Quaternary International* 246(1-2), pages 324–343. DOI: 10.1016/j.quaint.2011.05.029.

Weller, D. J., M. E. de Porras, A. Maldonado, C. Méndez, and C. R. Stern (2019). "Petrology, geochemistry, and correlation of tephra deposits from a large early-Holocene eruption of Mentolat volcano, southern Chile". *Journal of South American Earth Sciences* 90, pages 282–295. DOI: 10.1016/j.jsames.2018.12.020.

White, J. D. and G. A. Valentine (2016). "Magmatic versus phreatomagmatic fragmentation: Absence of evidence is not evidence of absence". *Geosphere* 12(5), pages 1478–1488. DOI: 10.1130/GES01337.1.

Wilson, M. (1989). *Igneous petrogenesis A global tectonic approach*. Edited by M. Wilson. 1st edition. London, England: Chapman and Hall. DOI: 10.1007/978-1-4020-6788-4.

Zimanowski, B., R. Büttner, P. Dellino, J. D. L. White, and K. H. Wohletz (2015). "Magma–Water Interaction and Phreatomagmatic Fragmentation". *The Encyclopedia of Volcanoes*. Elsevier, pages 473–484. DOI: 10.1016/B978-0-12-385938-9.00026-2.